Chapter 6

Semiconductor Fluoroprobes near Metal Nanostructures

Semiconductor Fluoroprobes near Metal Nanostructures

Semiconductor quantum dots were first introduced to biological imaging in 1998, as fluorophores with properties that give them tremendous advantages over the traditional organic dyes. Since then, much progress has been made in exploring their role in nanobiotechnology and nanomedicine as tools for diagnostic and therapeutic applications. The creation of hybrid metal-probe nanocomposites has paved an effective approach for producing enhanced or new physicochemical properties due to synergistic effects between different components. Because of the high chemical and photochemical stability of ZnO QDs deserves the possibility of using the semiconductor particles as efficient photoluminescent labels, the spectral changes upon addition of gold and silver nanoparticles could be probed by photoluminescence spectroscopy. Due to the advancement of synthetic strategies, the fluoroprobes may be isolated or aggregated. In this chapter, we have tried to elucidate the photoluminescence behavior of isolated and aggregated ZnO quantum dots in the presence of gold and silver nanoparticles, respectively. This chapter is divided into two sub-sections:

6.1. Manipulating Electron Transfer in ZnO-Au Nanohybrids

6.1.1. Introduction

In recent years, creation of hybrid nanocomposites has paved an effective approach not only for harvesting multifunctionalities contributed from each component but also producing enhanced or new physicochemical properties due to synergistic effects between differentcomponents.[1,2] These nanohybrids exhibit new optical, electrical, magnetic, mechanical, chemical and thermodynamic properties that can be tuned by controlling their composition, size, shape and organisation at the nanoscale.[3,4] The tunable properties along with the chemical and biological accessibility open up new opportunities to widespread their interest in a diverse range of niche applications.[5] The design and fabrication of semiconductor–noble metal hybrid nanocrystals with controlled morphologies imbue significant interest in designing advanced optoelectronic and

nanophotonic devices, such as, plasmonic nanolasers, plasmon-enhanced light emitting diodes and solar cells, plasmonic emitter of single photons, and quantum devices operating in infrared and terahertz domains.[6]

Amongst the semiconductors, zinc oxide (ZnO) at the nanoscale dimension has attracted immense interest due to its direct wide band gap (3.37 eV), high exciton binding energy (60 meV), the ease of synthesis due to its structural flexibility, and the opportunity to vary its properties by morphological tuneability.[7] Moreover, the unique physicochemical properties, such as, a range of conductivity from metallic to insulating, high transparency, room-temperature ferromagnetism, piezoelectricity, and huge magnetooptic and chemical sensing effects deserves the possibility of using ZnO nanoclusters in optoelectronics, catalysis, sensors, transducers, and biomedical sciences.[8] On the other hand, gold, at the nanometer size regime, exhibit characteristic surface plasmon resonance in the visible-NIR region that is absent in the individual atom as well as in their bulk.[9] Furthermore, many excellent properties, such as, easy reductive synthetic strategy to desired morphology, water-solubility, high conductivity, high chemical stability, significant biocompatibility and rich surface chemistry of nanoscale gold particles have encouraged their utilisationsin areas, such as, ferrofluids, medical imaging, drug targeting and delivery, cancer therapy, and catalysis.[10] Based on these perspectives, the construction of hybrid assemblies by self–organisation of semiconducting ZnO and plasmonic Au particles is important as the transfer of electrons from plasmon resonant metal surfaces to adjoining semiconductors can dramatically alter their electronic and optical properties and expand the scope of exploring composite nanoclusters in numerous technological applications. A plethora of research activities on ZnO–Au heterostructures have been pursued for the investigation of the physicochemical properties, such as, ultrafast separation of photogenerated charge carriers,[11] resonance multiphonon Raman signal[12] and formation of Schottky barrier due to partial charge transfer between the metal and the support[13] and exploring possible applications in voltammetry,[14] plasmon-induced switching,[15] photocatalysis,[16-18] biosensing,[19] diagnosis[20] and so on. Therefore, although many milestones have been crossed in this research arena, the interaction parameters of the binding of the individual components in the

heterostuctures in modulating the properties should be investigated to enrich the materials chemistry perspectives.

In this sub-section, we have studied the interaction parameters and band gap tuneability of water-soluble ZnO–Au nanocomposites by deposition of ZnO QDs onto size-specific gold nanoparticles and their correlation with the photocatalytic activity towards the degradation of dye molecules under visible light irradiation. Aqueous dispersion of size-specific gold nanoparticles and ultrasmall ZnO particles have been synthesised by wet chemical approach and subsequently, the nanocomposites were prepared by mixing the metallic and semiconductor particles at a particular composition. The binding of ZnO QDs to the size-specific gold nanoparticles has been characterised by absorption, photolumincence, and Raman spectroscopy, Fourier transform infrared spectroscopy, cyclic voltammetry and their morphology and crystallinity have been elucidated by transmission electron microscopy, high resolution transmission electron microscopy, selected area electron diffraction and X-ray diffraction techniques. All these characterisation techniques, unanimously, reflect the strong interfacial interaction between ZnO and Au in the nanohybrids and points out to the possibility of band gap tuneability by varying the size of the gold in the semiconductor-metal nanocomposites. Finally, the tuneability of the band gap of these nanohybrids has been probed by studying the degradation of Evans blue under visible light irradiation.

6.1.2. Experimental

6.1.2.1. Synthesis of ZnO Quantum Dots and Size-Specific Gold Nanoparticles

The synthesis of ZnO QDs and monodispersed gold nanoparticles of five different sizes has been carried out as described in detail below.

6.1.2.1.1. Synthesis of ZnO Quantum Dots

The synthesis of ZnO QDs has been carried out in an one-pot reaction by following the recipe of Weller group.[21] An aliquot of 0.055 g $Zn(OOCCH_3)_2.2H_2O$ was dissolved in 25 mL of methanol in a double-necked round-bottom flask by refluxing the mixture on a water bath at 45°C for 45 min and after that, the temperature was increased to 60 °C. After 15 min, 13.5 mL methanolic KOH solution (0.1 mM) was added to the reaction mixture instantaneously and refluxing was continued for another 2 h. A curdy white precipitate so formed slowly transformed to a faint yellow coloration indicating the

formation of ultrasmall ZnO particles. Then, the heating was stopped and the mixture was stirred for 12 h at room temperature. The ZnO nanoparticles so obtained were retrieved from methanol by centrifugation at 10,000 rpm for 15 min and were, subsequently, redispersed into water. The ZnO nanoparticles prepared by this method can be stored in the dark for several weeks without any significant agglomeration or precipitation of the particles.

6.2.1.2. Synthesis of Size-Specific Gold Nanoparticles

Monodispersed gold nanoparticles of five different sizes have been prepared by Frens' citrate reduction method.[22] In this method, it is possible to control the size of the particles by varying [Au(III)]/[citrate] ratio during the reduction step. A standard procedure for the preparation of set B is as follows. A 50 mL aqueous solution of $HAuCl_4$ (0.25 mM) is heated to boiling and 1.6 mL of trisodium citrate (1%) is added. In about 25 s, the boiling solution turns faintly blue (nucleation); after approximately 70 s, the blue color suddenly changes into a brilliant red, indicating the formation of gold particles. A lexicon of the synthetic conditions, UV-vis spectral characteristics and sizes for different sets of gold particles from transmission electron microscopic studies has been enunciated in Table 6.1.

Table 6.1. Synthetic Conditions[#] and Characteristic Parameters of the Size-specific Gold Nanoparticles

Set	Amount of $HAuCl_4$ solution (10 mM, mL)	Amount of trisodium citrate solution (1%, mL)	Colour	λ_{max} (nm)	Diameter (nm)
A	1.25	2.0	dark red	518	8.0 ± 1.0
B	1.25	1.6	red	519	10.0 ± 1.5
C	1.25	1.3	red	520	13.0 ± 2.0
D	1.25	1.0	red	522	16.0 ± 2.5
E	1.25	0.75	red	528	25.0 ± 3.0

[#] Total volume of the solution was maintained to 50 mL.

6.1.2.2 Making Semiconductor-Metal Nanohybrids

The preparation of ZnO QDs has been carried out by following the recipe of Weller group[21] and monodispersed gold nanoparticles of five different sizes by Frens' citrate reduction method[22] as has been described above in details. Then, semiconductor-metal

hybrid assemblies have been synthesised by gentle mixing of an aliquot of as-prepared ZnO QDs (16.7 µM) with Au NPs (0.67 µM) of 8, 10, 13, 16 and 25 nm in diameter in different vials to maintain the final volume at 3 mL and were allowed to incubate for overnight under vacuum. The colour of the dispersion was changed from red to redish pink to pink at the end of the reaction. The as-synthesised ZnO–Au nanohybrids were, then, employed for further studies.

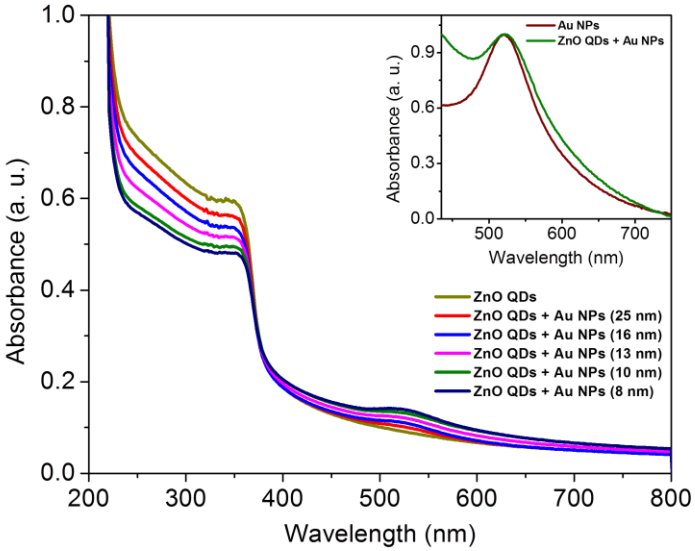

Figure 6.1. Absorption spectra of ZnO QDs (16.7 µM) in the absence and presence of Au NPs (0.67 µM) of five different sizes. Inset shows the change in the surface plasmon band of Au NPs (set B) upon interaction with the ZnO QDs.

6.1.3. Results and Discussion

The changes in the optical characteristics in the formation of ZnO–Au NCs by self-organisation of metallic and semiconductor nanoparticles have been elucidated by absorption, photoluminescence, and Raman spectroscopy. The absorption spectra of pure ZnO QDs and those after addition of five different sizes of Au NPs are shown in Figure 6.1. The absorption peak of pure ZnO QDs at around 350 nm (3.54 eV) could be attributed to the well-defined exciton band of the ultrasmall particles.[23] Upon addition of gold colloids, it is seen that the excitonic band of ZnO becomes red shifted and in addition, a weak band becomes visible in the range of 500 –550 nm (2.48 – 2.25 eV) that arises due to the localised surface plasmon resonance of spherical gold nanoparticles.[9] The appearance of surface plasmon band reveals the presence of metallic gold in Au–ZnO nanocomposites. Upon careful observation, it is noted that the excitonic band of ZnO, consecutively, shifts towards the red and the plasmonic band of gold shifts towards the blue as the size of the noble metal nanoparticles decreases. The red shift of the ZnO QDs upon addition of gold colloids reflects the strong interfacial interaction between

semiconductor ZnO and metallic Au components in producing new heterostructures.[24] Inset shows the change in the surface plasmon band of gold nanoparticles (set B) upon addition of ZnO QDs. The surface plasmon band of gold sol (trace a) exhibits a maximum at 519 nm (2.39 eV). When ZnO QDs are added to the gold sol (trace b), the plasmon band of the metal particles broadens and shifts towards higher wavelengths at 521 nm (2.38 eV).[25] It is known that the position of the surface plasmon band depends on the conduction band electron density.[9] The interfacial interaction between ZnO and Au leads to charge variation of the Au surface which is the cause of the red shift of the Au surface plasmon band in the ZnO–Au NCs.[26] Since the Fermi energy level of gold is higher than that of ZnO, a consequence of the fact that the work function is smaller for gold[27] (5.1 eV) than for ZnO[28] (5.2–5.3 eV), electron transfer occurs from Au to ZnO during the formation of ZnO-Au NCs until the two systems attain equilibration.[29] The deficient electrons on the Au surface, consequently, induce the broadening and red shifting of the surface plasmon band, consistent with previous reports that Au electron deficiency shifts the surface plasmon band to a longer wavelength.[30]

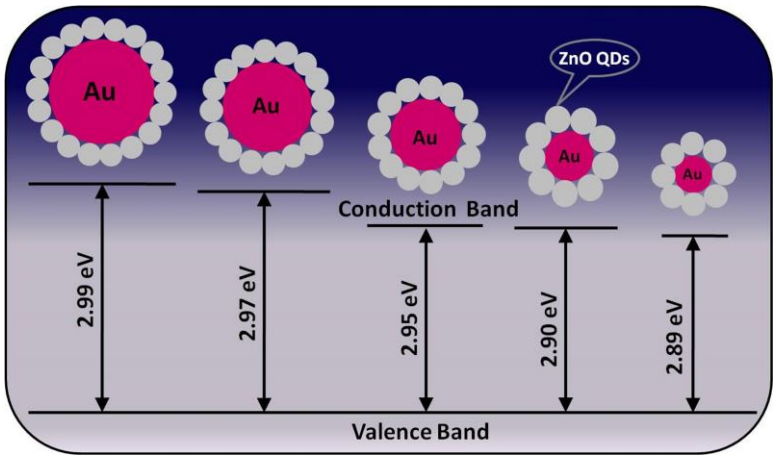

Scheme 6.1. Schematic presentation of miniaturising the band gap in ZnO–Au nanohybrid assemblies containing Au NPs of five different sizes.

The engineering of band gap is a common practice for tuning semiconductors for desired physical properties.[31] The electronic structure of semiconductors, such as, ZnO is characterised by a valence band, which is filled with electrons, and an empty conduction band. In semiconductor–metal nanocomposites, the photoinduced charge carriers are trapped by the noble metal nanoparticles and become able to promote the interfacial charge–transfer processes.[32] Although, the band gap of ZnO QDs has been calculated to be 3.03 eV, the values of band gap are reduced to *ca.* 2.89, 2.9, 2.95, 2.97 and 2.99 eV in attachment with the gold

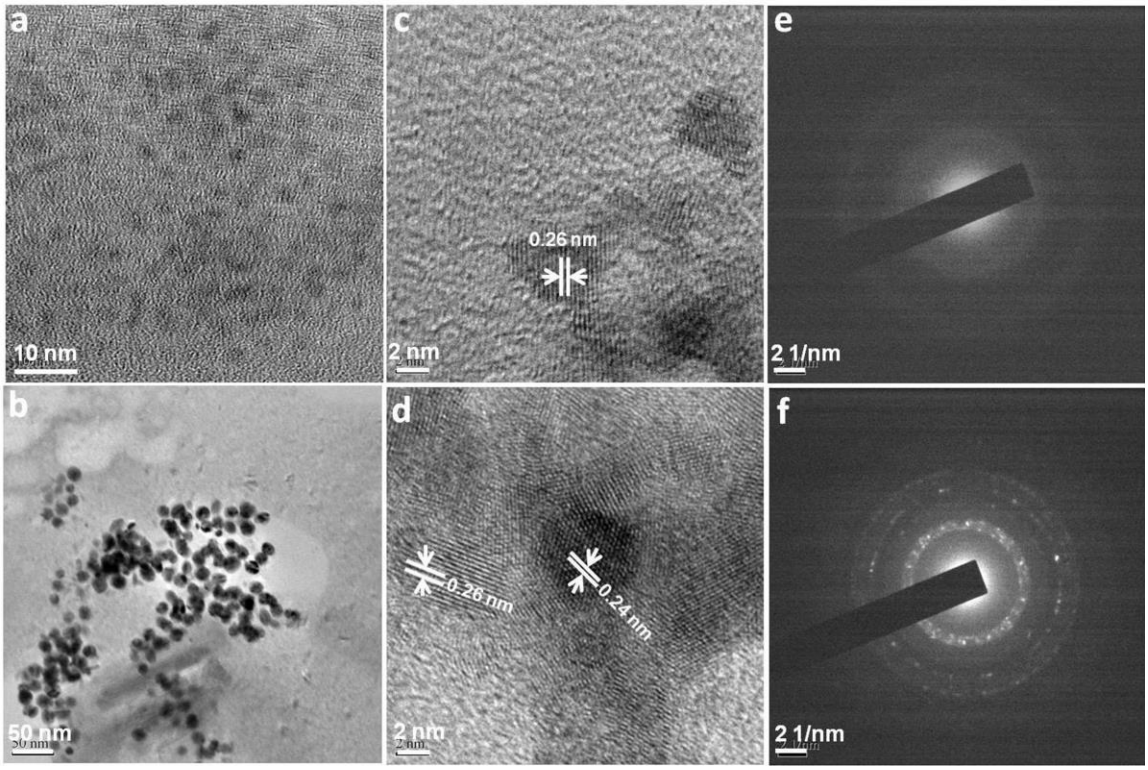

Figure 6.2. (a, b) Transmission electron micrographs, (c, d) high resolution transmission electron micrographs and (e, f) selected area electron diffraction pattern of ZnO and ZnO−Au, respectively.

nanoparticles of sizes 8, 10, 13, 16 and 25 nm, respectively. Thus, manipulating and guiding photons at the nanoscale inside semiconductor could, sensitively, be managed with the assistance of plasmonics.[33] A picturesque detail of the energy band diagram of the semiconductor–metal nanocomposites consisting of ZnO QDs and Au nanoparticles of variable sizes has been presented in Scheme 6.1.

The morphology and crystallinity of the ZnO QDs and representative ZnO–Au NCs (containing Au NPs from set B) have been illustrated in Figure 6.2. Transmission electron micrograph of ZnO QDs (panel a) shows that particles are quasi-spherical with average diameter 3 ± 0.5 nm. Representative TEM image of the ZnO–Au NCs (panel b) clearly displays a high coverage of ZnO QDs deposited on the surfaces of the Au NPs with overall diameter *ca.* 16 ± 4 nm. Typical high resolution TEM image of ZnO QDs (panel c) shows the distance between two adjacent planes as 0.26 nm, corresponding to (002) planes in wurtzite ZnO.[34] The high resolution image of ZnO–Au NCs (panel d) exhibits the distance between two adjacent planes in wurtzite ZnO as 0.26 nm,

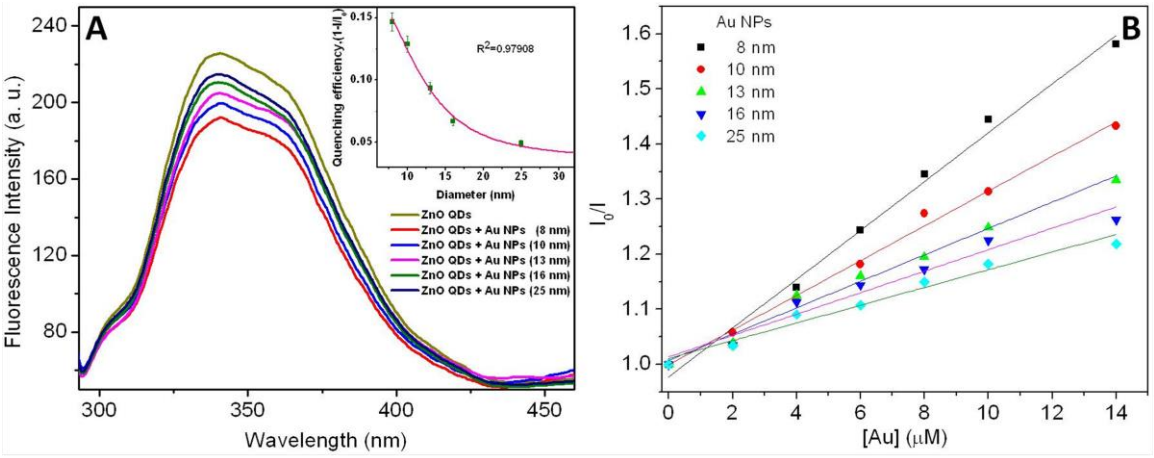

Figure 6.3. (A) Fluorescence spectra of ZnO QDs (16.7 μM) in the absence and presence of Au NPs (0.67μM) of five different sizes. Inset shows the quenching efficiency of the Au NPs as a function of particle size. (B) Stern –Volmer plots of the quenching of ZnO QDs (16.7 μM) upon addition of five different sizes of Au NPs.

corresponding to (002) planes, and that in fcc structured Au as 0.24 nm, resulting from a group of (111) planes.[34] The naked eye visualisation of the image distinguishes the high contrast difference between ZnO and Au because of the higher electron density of metallic Au and the well-proportioned brightness reveals the presence of ZnO entirely covered on metal particle's surface with high regularity and uniformity.[34] From the selected area electron diffraction pattern of ZnO QDs (panel e), the diffraction rings which are consistent with reflections (100), (002), (101), (102), (110) corresponds to the hexagonal wurtzite phase of ZnO nanoparticles.[34] The corresponding SAED pattern of ZnO–Au NCs (panel f) exhibits the appearance of polycrystalline-like diffraction which reveals the diffraction patterns for both ZnO and Au in the assemblies.[34]

Since the high chemical and photochemical stability of the ZnO QDs deserves the possibility of using the semiconductor particles as efficient photoluminescent labels,[35] the spectral changes upon addition of gold nanoparticles could be probed by photoluminescence spectroscopy (Figure 6.3). It has been seen that the photoluminescence spectrum (λ_{ex} ~ 276 nm) of the ZnO particles at the nanoscale dimension exhibits a narrow near-band-edge UV emission with maximum at 350 nm (3.54 eV) and a weak broad green band with maximum at 540 nm (2.3 eV). The ultraviolet emission peak corresponds to an excitonic emission that could be attributed to

the radiative recombination of a hole in the valence band and an electron in the conduction band;[35] whereas, the broad green emission band, known as a deep-level emission, is believed to be due to an electronic transition from a level close to the conduction band edge to a defect associated trap state, such as, oxygen vacancies, zinc vacancies, as well as donor–acceptor pairs.[35] Panel A shows the room temperature excitonic emission spectra (λ_{ex} ~ 276 nm) of pure ZnO QDs and ZnO–Au NCs evolved upon addition of five different sizes of gold nanoparticles. Upon addition of gold colloids, it is seen that the intensity of the UV emission is significantly quenched than that of the pure ZnO QDs, indicating the decreased electron-hole combination.[36] It is to be noted that gold nanoparticles, are themselves non-photoluminescent. The photoluminescence quenching of ZnO QDs could be attributed to the strong interfacial interaction between ZnO and Au particles.[37] Upon excitation, the plasmonic state of gold interacts with the excited state of semiconductor that provides an avenue for the delocalisation of photogenerated electrons. Therefore, electron transfer, preferably, occurs from the semiconductor to the metallic gold in the nanocomposites that seems to quench the ZnO emission. Moreover, it is seen that extent of quenching decreases with increase in size of the gold particles in the ZnO–Au NCs, particularly, quenching efficiency decreases exponentially with the particle diameter as shown in the inset. The Stern-Volmer quenching constant, K_{SV} accounting both static and dynamic quenching is related to the photoluminescence efficiency via the relationship as, $\frac{I_0}{I} = 1 + K_{SV}[Quencher]$, where, $K_{SV} = K_S + K_D$ and K_S and K_D are the static and dynamic quenching constants respectively.[38] Panel B shows the profiles of I_0/I *vs.* gold concentration for a fixed concentration of ZnO QDs (16.7 μM) and corresponding K_{SV} values are determined as 4.434×10^4, 3.155×10^4, 2.398×10^4, 1.947×10^4 and 1.609×10^4 M^{-1} for gold particle sizes as 8, 10, 13, 16 and 25 nm, respectively. It is noted that Stern-Volmer quenching constant increases by nearly three-fold when the gold particle size decreases from 25 to 8 nm in the ZnO–Au NCs. This indicates that the electron transfer is pronounced for smaller particles as they have high surface area/energy and relatively more electronegative and therefore, possess high tendency to accept electrons. Therefore, smaller particles of gold are effective quenchers of photoluminescence of ZnO QDs than the larger ones. However, these results are in contrast to the observation of

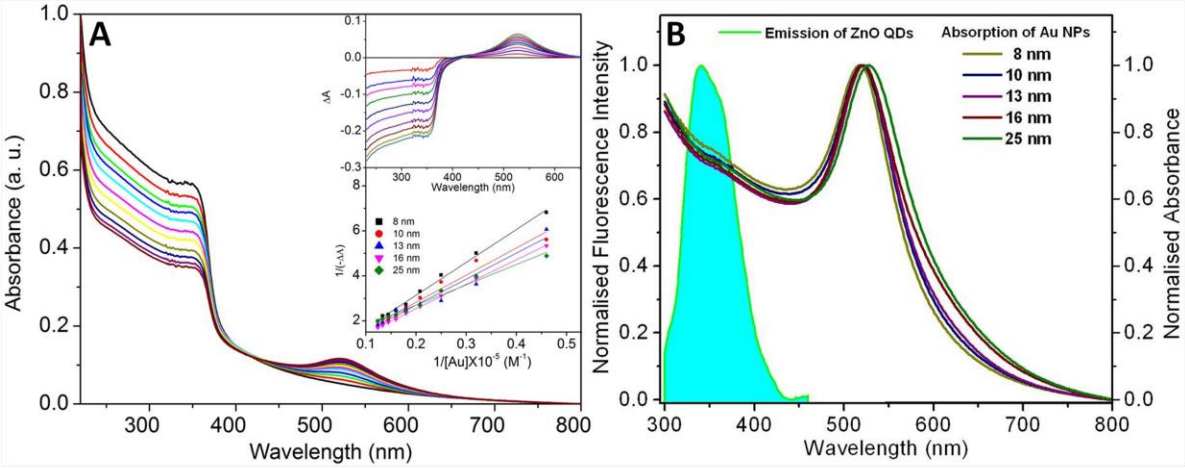

Figure 6.4. (A) Absorption spectral changes of ZnO QDs (16.7 μM) upon successive addition of gold nanoparticles (set B) (4 – 40 μM). Inset shows the profile showing dependence of 1/(-ΔA) as a function of 1/[Au NPs]. (B) Overlap between the UV emission spectrum of ZnO QDs (16.7 μM) with absorption spectra of gold nanoparticles (40 μM) of five different sizes.

plasmonic emission enhancement from quantum dots near metallic nanostructures as has been elucidated by several groups due to coupling with surface plasmon resonance of the metallic particles.[39-41]

Now, we have tried to elucidate the mechanism of fluorescence quenching between photoluminescent semiconductor and plasmonic metal nanostructures (Figure 6.4). Both electron and energy transfer processes are perceived to be the major deactivation pathways for excited photoluminescent probes on the metal surface. Panel A shows the absorption spectral changes of ZnO QDs upon successive addition of gold nanoparticles (set B). When an aliquot of Au NPs is added to an aqueous dispersion of ZnO QDs, the absorbance of the semiconductor particles decreases and new band evolves in the range of 500 – 550 nm (2.48 – 2.25 eV) corresponding to the surface plasmon absorption of gold nanoparticles. As the concentration of Au NPs increases, the intensity of the excitonic band of ZnO QDs gradually decreases with stepwise red shifting and the surface plasmon absorption gradually develops. This can be ascribed to the fact that electron transfer from the conduction band of ZnO to Au due to the formation of the metal–semiconductor interface. The gold atoms on the surface possess high residual force and unoccupied orbitals to accept electrons from nucleophiles and this has been satisfied

by ZnO providing the electrons to the gold surface.[12,25] A plot of ΔA as a function of wavelength, as shown in the inset (top), exhibits the presence of an isosbestic point at *ca.* 410 nm which confirms that these absorption changes arise from a complexation equilibrium between the ZnO QDs and Au NPs. The spectral changes can be used to assess the apparent association equilibrium under the experimental conditions. The apparent association constant (K_{app}) for the complexation between ZnO QDs and Au NPs could be obtained by analysing the absorption changes similar to a Benesi-Hildebrand approach.[42] The double reciprocal plot of 1/(-ΔA) *vs.* 1/[Au NPs], as shown in the inset(bottom), gives an apparent association constant of the binding of ZnO QDs to the Au NPs (set B). Thus, the values of K_{app} have been *ca.*14.6178×10^5, 12.0505×10^5, 11.5555×10^5, 10.8647×10^5 and 9.0363×10^5 for gold particle sizes as 8, 10, 13, 16 and 25 nm, respectively. The high values of K_{app} suggest strong association between the ZnO QDs and Au NPs of different sets. In addition, the salient feature of physical significance is that the apparent association constant for ZnO–Au depends on the size of the particles and increases as the size of the gold particles decreases, further, authenticating the strong binding of the ZnO QDs with the smaller metallic particulates.[43]

Quenching may also take place when the ZnO QDs are placed in the vicinity of a metal surface through an additional nonradiative decay channel via resonance energy transfer to metal nanostructures as has been seen in many metal–semiconductor nanocomposites, such as, Ag–ZnO, Au–ZnO, Al–ZnO, Mg–ZnO and Pt–ZnO.[8] Förster resonance energy transfer (FRET) involves the nonradiative transfer of excitation energy from an excited donor to a ground state acceptor brought in close proximity, which can radiatively emit a lower energy photon.[44] Semiconductor ZnO QDs placed in the vicinity of Au NPs can transfer energy to the metallic nanoparticles once it gets excited. The energy transfer is believed to be through the dipole-dipole near-field interaction, where the semiconducting probes act as dipolar donors and the plasmonic gold nanostructures act as dipolar acceptors.[45] The probability of this Förster resonance energy transfer is proportional to the spectral overlap between the absorption of the metallic nanostructures and the photoluminescence emission of the ZnO QDs.[44] Panel B shows the overlap between the absorption spectrum of gold nanoparticles and the photoluminescence spectrum of ZnO QDs. It is seen that there is no significant overlap between

photoluminescence spectrum of ZnO QDs (300-450 nm region) and absorption spectrum of gold NPs (300 – 800 nm region). As a result, the Au NPs could not absorb the emitted light, significantly, from the ZnO QDs and therefore, impart a negligible contribution to the quenching efficiency of the ZnO QDs. Thus, overall very small quenching is observed perhaps only due to the electron transfer from ZnO QDs to the metallic nanostructures.[46]

Figure 6.5 represents the FTIR spectra of ZnO QDs before and after addition of gold nanopartcles. The FTIR spectrum of ZnO (trace a) shows the main absorption band arising at *ca.* 462 cm^{-1}, could be assigned to stretching vibration of Zn–O bonds; the other absorption band at 1263 cm^{-1} corresponds to C–O stretching frequency due to adsorbed acetate counter ions.[47] The appearance of weak bands in the region 1500–3500 cm^{-1} could be assigned to the stretching and bending modes of coordinated water molecules.[47] Upon addition of colloidal gold to the ZnO QDs (trace b), the band at 462 cm^{-1} is shifted to 458 cm^{-1} corresponding to Zn–O stretching vibration and the appearance of new band at 437 cm^{-1} could be attributed to the characteristic stretching modes of Au–O bonds.[48] The presence of extra bands at 1395 and 1663 cm^{-1} could be attributed to the asymmetric and symmetric COO^- stretching vibration of citrate, adsorbed onto the gold surface.[49] The absorption bands at *ca.* 869 and 3165 cm^{-1} could be assigned to the stretching modes of O–H groups that reveals the existence of small amount of water physisorbed and/or chemisorbed by the ZnO–Au nanocomposites.[50] The changes in the FTIR spectrum upon

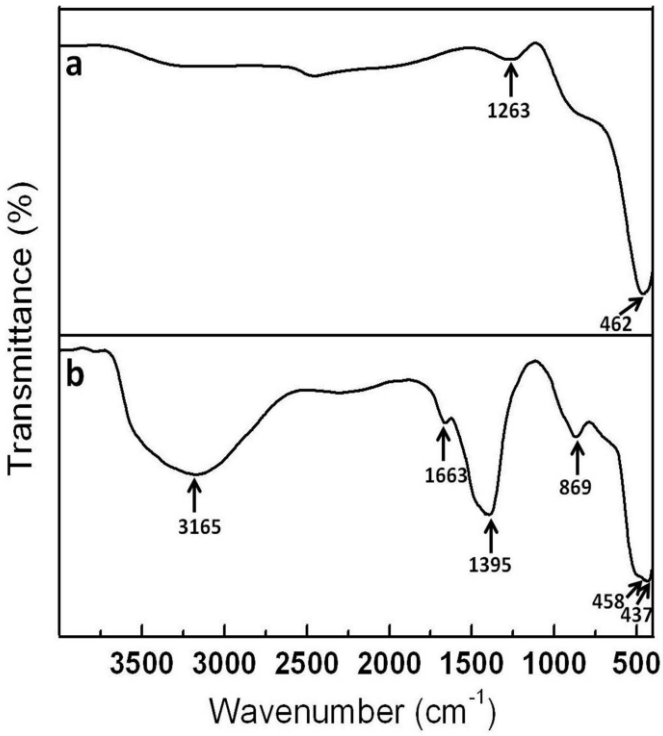

Figure 6.5. Fourier transform infrared spectra of the as-prepared (a) ZnO QDs and (b) ZnO–Au NCs.

addition of gold colloids indicates the binding of metallic particles with the zinc oxide nanostructures. Cyclic voltammograms of ZnO QDs (1.67 mM), Au NPs (0.067 mM), and ZnO–Au NCs (molar ratio 25 : 1) in different potential windows is shown in Figure 6.6. The observed anodic peak potential (E_{pa}) of the Au NPs, ZnO QDs and ZnO–Au NCs is measured to be –0.37, –0.45 and –0.40 V, respectively. From these data, it is noted that the anodic peak potential is in the order of Au NPs < ZnO–Au < ZnO QDs, i. e., the anodic/oxidation potential is less in composites as compared to ZnO QDs while high with respect to Au NPs. It is, therefore, revealed that the charge transfer takes place from ZnO QDs to Au NPs, which reduces the potential differences between the two components in ZnO–Au NCs.[14] Again, in the reverse scan, the cathodic peak potential (E_{pc})/reduction potential of ZnO–Au NCs (–0.11 V) is lesser with respect to ZnO QDs (–0.10 V) (though the difference is a small quantity) implies that charge transfer takes place from Au to ZnO in the ZnO–Au composites. Moreover, the anodic peak current (i_{pa}) of 24.99 and 19.77 μA of ZnO QDs and ZnO–Au NCs, respectively represents the charge transfer is very high that exhibits the extent of electron transfer is more from ZnO to Au in the composites. On the otherhand, the value of cathodic peak current (i_{pc}) of –3.67 and –1.87 μA of ZnO QDs and ZnO–Au NCs, respectively reveals that the charge transfer is very less in ZnO–Au composites than in ZnO QDs. Since, the

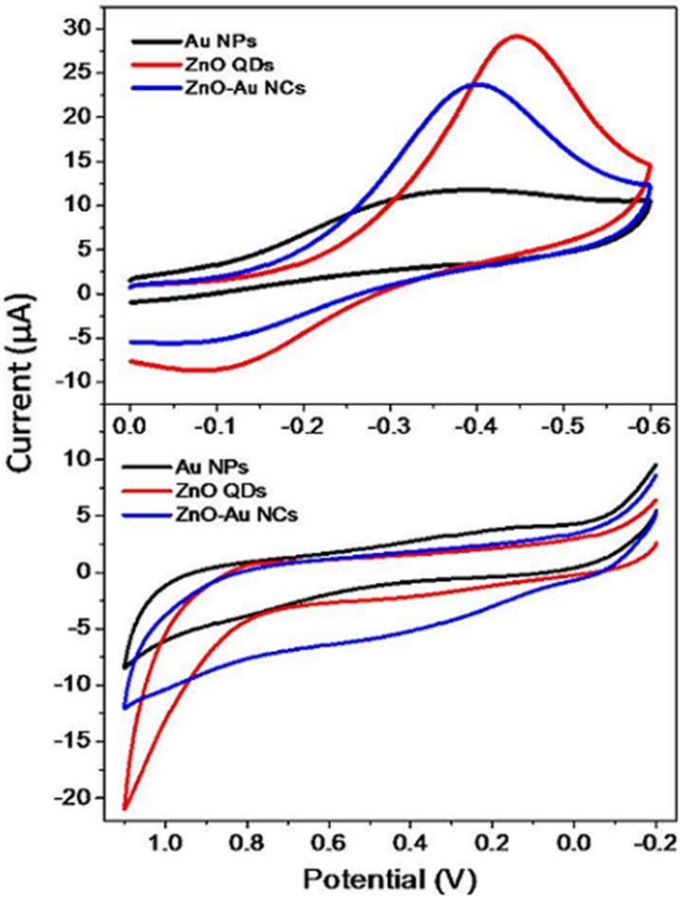

Figure 6.6. Cyclic voltammograms of ZnO QDs (1.67 mM), Au NPs (0.067 mM), and ZnO–Au NCs (molar ratio 25 : 1) in 0.1 M KCl solution in different potential windows.

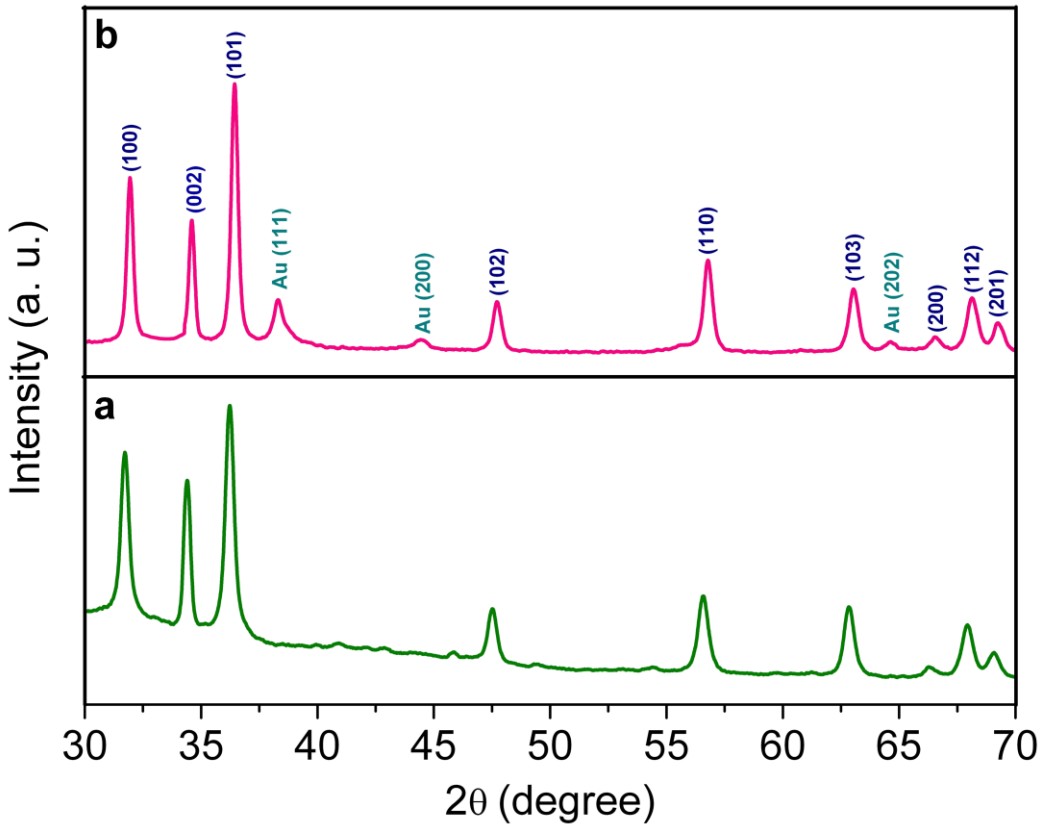

Figure 6.7. X-ray diffraction pattern of the as-prepared (a) ZnO QDs and (b) ZnO–Au NCs.

potential difference indicates the direction of flow of charge and the amount of current reflects the quantity of charge transfer, therefore, it could be concluded that the charge transfer is a reversible process, though the extent of charge transfer is more in ZnO→Au than in the reverse order Au→ZnO in the ZnO–Au nanocomposites.[51]

Powder X-ray diffraction patterns of pure ZnO QDs and ZnO–Au NCs are shown in Figure 6.7. All the diffraction peaks of trace a could be indexed as pure hexagonal phase of Zn with a space group of C_{6v}^{4} and cell constants a = 3.25 Å, and c = 5.21 Å (JCPDS Card No.: 76-0704), which suggests that the product could be classified as the wurtzite phase of ZnO nanostructures.[25] After the deposition ZnO QDs on the surface of gold nanoparticles (trace b), the XRD pattern exhibits broad and relatively weak diffraction peaks that could be assigned to the wurtzite-type ZnO (JCPDS Card No.: 76-0704) and weak metallic gold diffraction lines are also evidenced corresponding to the face-centred

cubic Au (JCPDS Card No.: 65-2879); the absence of any other peak in the diffraction pattern indicates the absence of any other crystalline impurities in the ZnO–Au NCs.[25]

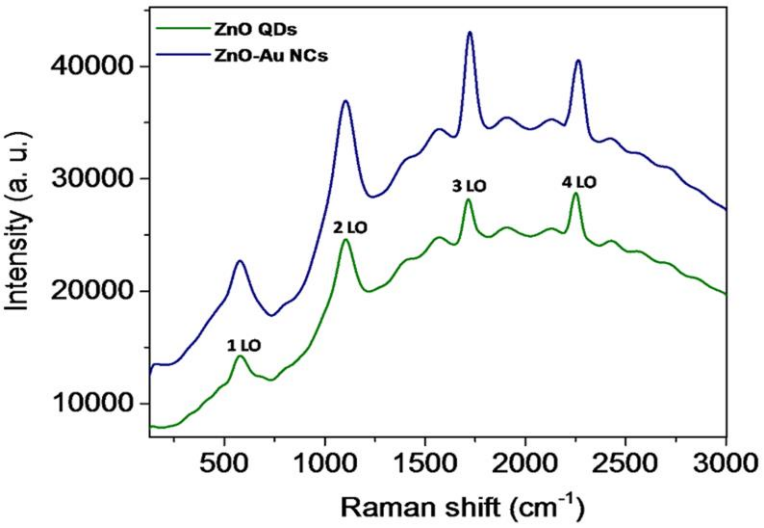

Figure 6.8. Enhanced multiphonon Raman scattering spectrum of ZnO QDs and ZnO–Au NCs.

Raman spectroscopy is the most powerful investigation technique to achieve sensitive detection of optical phonon modes and therefore, to characterize related vibrational properties.[52] In the present experiment, the samples were excited by the 488 nm (2.55 eV) line of a Ar^+ laser; multiphonon scattering[53] is, therefore, observed in the Raman spectra of pure ZnO QDs and ZnO-Au NCs as shown in Figure 6.8. The structure of ZnO belongs to the C_{6v}^4 symmetry group having two formula units per primitive cell with all the atoms occupying the C_{3v} sites, which predicts eight sets of zone centre optical phonons: two A_1, two E_1, two E_2 and two B_1 modes. Among these, A_1 and E_1 modes are polar and split into transverse (A_1T and E_1T) and longitudinal (A_1L and E_1L) phonons, all being Raman and infrared active; E_2 modes are non-polar consisting of two modes of low- and high-frequency (E_2L and E_2H) phonons and are only Raman active, and B_1 modes are infrared and Raman inactive (silent modes).[53] The frequency of the first-order Raman mode at 577 cm^{-1} is between the A_1 (LO) mode (574 cm^{-1}) and the E_1 (LO) mode (591 cm^{-1}), which is a simple sum of both Raman signals and the frequency shifts are multiples of 1-LO zone-center frequency of 577 cm^{-1}. It is seen that there are four major sharp bands of longitudinal optical (LO) phonons where, the *n* LO refers to the *n*th longitudinal optical phonon. Upon addition of gold colloids, all the frequencies of pure ZnO shifts from original positions indicating the attachment of ZnO QDs to the Au NPs.[25] Moreover, it is interesting to note that the multiphonon Raman scattering is also, largely, enhanced in the ZnO–Au NCs in comparison with the pure ZnO QDs. This could be ascribed to the fact that the electrons

transferred from ZnO QDs to the Au NPs can yield the electromagnetic field enhancement of the gold surface plasmon, which, further, enhances the multiphonon Raman scattering of the semiconductor particles.[54]

In the present experiment, both ZnO (due to the adsorption of negatively charged acetate counter ions) and Au (due to the adsorption of negatively charged citrate counter ions) are negatively charged. A plausible mechanism of the binding of ZnO QDs onto the surface of citrate-stabilized gold nanoparticles could be enunciated as follows. In the trisodium citrate solution (pH ~ 8.0), ZnO nanoparticles are positively charged because the PZC (point of zero charge) of ZnO is 11.0 and therefore, becomes attached onto the negatively charged Au nanoparticles through electrostatic interaction.[55] The electrostatic binding of ZnO QDs onto the surface of Au NPs enhances the stability of ZnO−Au NCs and enables the nanocomposites to be stably dispersed in the aqueous media for more than 6 months.[55]

Photocatalysis, where photons are used for catalytically activating chemical reactions on the surface of photosensitized catalysts, remains one of the leading hubs of research for harvesting the solar light.[56] Typically, photocatalysts generate the charge carriers on excitation and under suitable conditions, these are transferred from the catalysts to the reaction medium, which, in turn, initiate the chemical reaction.[56] It has now, commonly, been experienced that small transition metal clusters exhibit their chemical behavior as photocatalysts. Nevertheless, ZnO has received strong attention as promising photocatalyst due to its innocuousness, abundance, facile synthesis allowing for versatile shapes and sizes, and its easy surface modification.[7] But the major drawback for exploiting their utility under visible light irradiation is that the optical absorption of these materials lies in the UV range of the solar spectrum due to the wide band gaps of more than 3.0 eV so that only a small part of the incident energy can be converted. However, this issue can be alleviated, significantly, by combining a semiconductor photocatalyst with tailored plasmonic nanostructures; the ability to donate or accept charge points to the utilization of such metal–semiconductor nanohybrids in photocatalytic applications.

Now, the catalytic activities of the ZnO–Au nanocomposites consisting of gold nanoparticles of variable sizes have been probed in photochemical decomposition of Evans blue under visible light illuminations as the model reaction. Evans blue

[Tetrasodium (6*E*,6'*E*)-6,6-{(3,3'-dimethylbiphenyl-4,4'-diyl)di(1*E*)hydrazin-2-yl-1-ylidene}bis(4-amino-5-oxo-5,6 dihydronaphthalene-1,3-disulfonate)], also known as 'Direct Blue 53', is a diazo dye and can be useful in physiology in estimating the proportion of body water contained in blood plasma.[57] Furthermore, they are used for colouring of rayon, paper, leather and to a less extent nylon; however, discharge of such colourants to surface water cause harmful environmental effects.[57] The photocatalytic degradation of Evans blue was employed as the model reaction as its degradation can, easily and quantitatively, be monitored via its absorption spectroscopy. Moreover, Evans blue was chosen because of its high stability against spontaneous photobleaching in the absence of a photocatalyst.[57] In the photocatalytic reaction, 33 μg of the as-prepared catalysts was dispersed with 3.0 ml of 20 μM aqueous solution of the dye molecules and the dispersion was stirred in the dark for 2 h to reach adsorption-desorption equilibrium between the catalysts and dye molecules. Then, the solution was irradiated with the tungsten lamp and the progress of the reaction was followed in the absorption spectrophotometer. The blank of the instrument was performed before addition of Evans blue but in the presence of ZnO–Au hybrid nanocrystals to eliminate the contribution of the plasmon resonance peak of Au. The photochemical degradation of the dye in the presence of different nanostructures is presented in Figure 6.9. Panel A shows the degradation of Evans blue in the presence of ZnO–Au NCs (containing Au NPs from set B). Aqueous solution of the dye molecules exhibit a very intense absorbance band centered around 608 nm corresponding to $n \rightarrow \pi^*$ transitions and molar extinction coefficient, $\varepsilon \sim 7.8 \times 10^4\ M^{-1}\ cm^{-1}$ corresponding to the monomeric form of the dye.[57] As controls, an aqueous solution of EB (3.0 ml, 20 μM) was exposed to the same tungsten lamp under identical experimental conditions. It was observed that, in the absence of the catalysts, the photochemical decomposition of the dye is not appreciable in the experimental time scale. In addition, it was noted that the decomposition of the dye is also very slow in the presence of pure ZnO QDs; however, the degradation becomes faster in the presence of ZnO–Au nanohybrids. These changes in the absorption spectral features indicate that with increase in irradiation time Evans blue undergoes photocatalytic degradation and forms small fragmented organic products.[58] The decrease in intensity of the absorption band of Evans blue at 608 nm has been used to access the

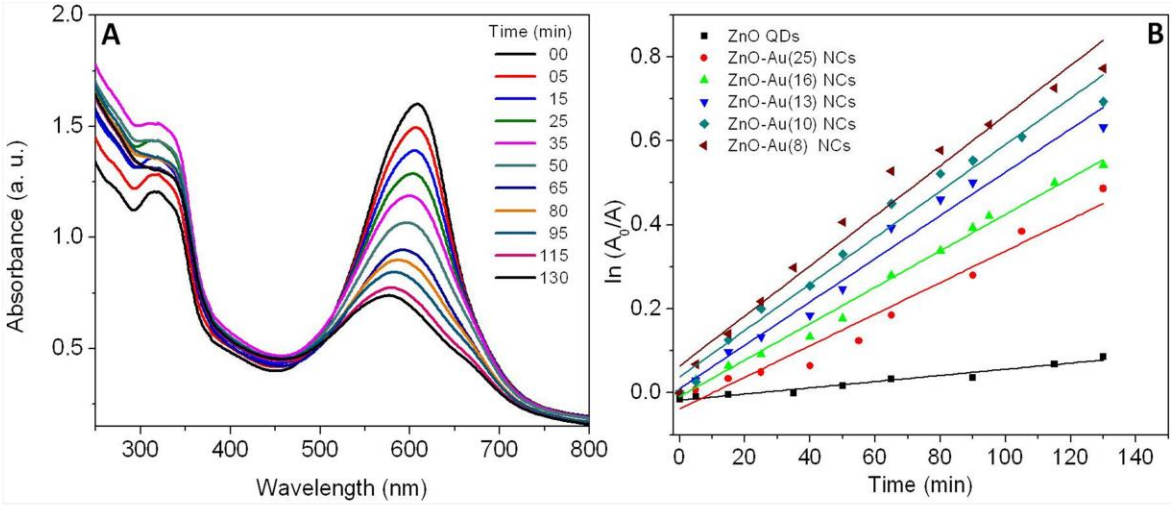

Figure 6.9. (A) Absorption spectral changes during the degradation of Evans blue (20 μM) in the presence of ZnO-Au NCs (containing gold nanoparticles from set B) upon visible light irradiation. (B) Profile showing the plot of $ln\left({}^{A_0}/_{A}\right)$ as a function of time for photocatalytic degradation of Evans blue in the presence of ZnO QDs and ZnO-Au NCs containing gold nanoparticles of five different sizes.

photocatalytic activity of the nanostructures for the degradation of the dye. A profile showing the plot of $\ln(A_0/A)$ where, A_0 is the absorbance at t = 0 and A the absorbance at time t = t, as a function of time as presented in panel B shows that the reaction follows first order kinetics and the corresponding catalytic rate constants (K_{cat}) have been calculated as 0.7×10^{-3}, 5.96×10^{-3}, 5.53×10^{-3}, 5.15×10^{-3}, 4.34×10^{-3} and 3.76×10^{-3} min^{-1} in the presence of pure ZnO and five different sets of ZnO–Au nanohybrids containing Au NPs of sizes 8, 10, 13, 16 and 25 nm, respectively. Thus, the design of semiconductor-plasmonic metal composites exhibit better photocatalytic activity in comparison with pure semiconductor for the degradation of Evans blue under visible light irradiation while all other parameters remain constants. It is, therefore, apparent that the deposition of ZnO QDs onto the surfaces of Au NPs significantly alters the interfacial charge transfer process and greatly affects their photocatalytic properties.[18] Moreover, it is noted that as the size of the gold particles in the ZnO–Au nanohybrids decreases, the photocatalytic activity increases as has been by Pradhan group employing Au–SnS heterostructures.[59]

The improved photocatalytic activities of ZnO–Au NCs in comparison with pure ZnO QDs could be accounted to three reasons. Firstly, ZnO QDs are not compatible in mixing with aqueous medium and sediment at the bottom of the container; whereas, the ZnO–Au NCs are easily dispersible in aqueous medium.[25,60] Secondly, the less electron density on the conduction band and homogeneous nature of electron cloud in ZnO QDs; however, these difficulties could be overcome in ZnO–Au NCs.[51] The gold part generates a heterogeneous environment through the formation of resonant surface plasmons of the free electrons in response to a photon flux, localizing electromagnetic energy close to their surfaces. Since, ZnO QDs are capable of transferring electrons to gold nanoparticles, there is the formation of a built-in electromagnetic field at the interface of ZnO–Au nanocomposites. This results in excitation and de-excitation of the electrons of the ZnO QDs attached onto the plasmonic gold surface which periodically increases/decreases the electron density in the conduction band of ZnO like a wave and as a result, the photocatalytic activity is enhanced.[61] Thirdly, the absorption of pure ZnO QDs falls in the UV region; since, visible light was incident for the catalysis during the experiments, therefore, practically no excitation takes place in the ZnO QDs that results to exhibit poor catalytic activity. But in the ZnO-Au NCs, due to the presence of nanostructured gold, the band gaps decreases which, further, allows the absorption of broad range of wavelengths of incident light. As a result, there is an increase in excitation

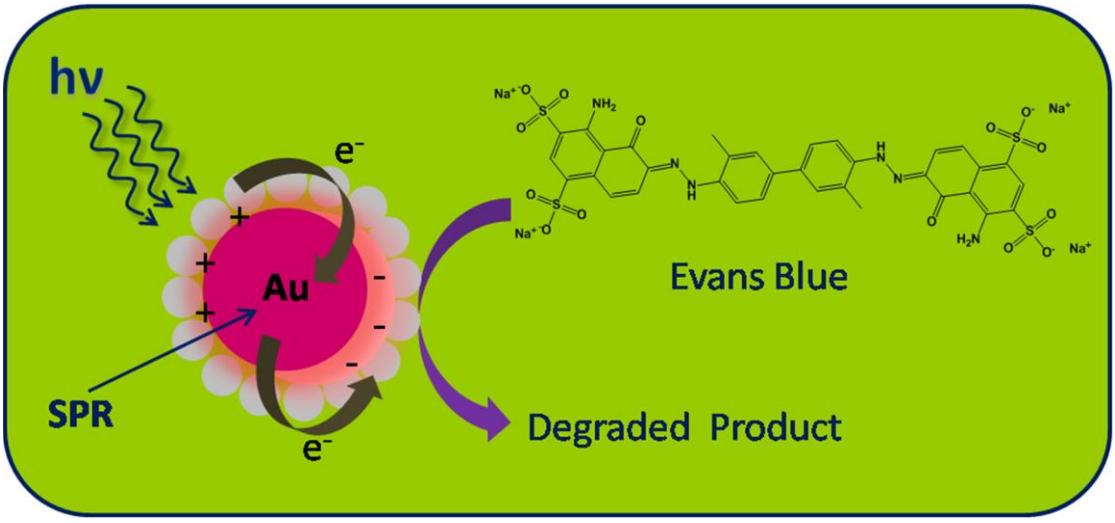

Scheme 6.2. Schematic presentation of the photocatalytic degradation of Evans blue at the ZnO-Au nanocomposites surfaces.

of electrons from the valence band to the conduction band in the ZnO part of the ZnO−Au NCs; the enhancement of electron density in the conduction band, further, increases the photocatalytic activity.[3] Therefore, a plausible mechanism of the photocatalysis by ZnO−Au NCs for the degradation of Evans blue under visible light irradiation could be enunciated as shown in Scheme 6.2.

When bulk materials are scaled down to the nanoscale, novel properties emerge, such as, size-dependent band gaps due to quantum confinement, enhanced catalytic properties due to the large surface area and rich surface structure, and plasmonic effects due to localized collective electron oscillation.[62] However, when these NPs are interacting with the nearby environment, as is inevitable in device applications, their intrinsic properties diverges from that of free particles and depends, critically, on the chemical composition and electronic properties of the adjacent materials.[63] In the present experiment, it is seen that the band gap of ZnO QDs could be varied upon adsorption onto the size-specific gold nanoparticles. The mechanism of tuning the band gap can be explained by the nature and extent of interaction between the ZnO QDs and Au NPs of different sizes in the composites. With decreasing the size of the gold nanoparticles, the extent of electrostatic interaction with the ZnO particles increases due to two reasons. Firstly, with decreasing

Table 6.2. Characteristic Physical Parameters as a Function of Gold Particle Size in ZnO-Au Nanocomposites

Diameter of gold particles, D_{Au} (nm)	Apparent association constant, K_{app} (M^{-1})	Stern-Volmer quenching constant, K_{SV} (M^{-1})	Band gap, E_g (eV)	Catalytic rate constant, K_{cat} (min^{-1})
8	14.6178×10^5	4.434×10^4	2.89	5.96×10^{-3}
10	12.0505×10^5	3.155×10^4	2.90	5.53×10^{-3}
13	11.5555×10^5	2.398×10^4	2.95	5.15×10^{-3}
16	10.8647×10^5	1.947×10^4	2.97	4.34×10^{-3}
25	9.0363×10^5	1.609×10^4	2.99	3.76×10^{-3}

size of the metallic nanoparticles, the surface-to-volume ratio increases and hence, large number of ZnO QDs could be attached onto the gold nanoparticle surfaces. Secondly, the total residual force (surface energy) increases with decreasing the size (as the number of particles increases for a particular gold concentration) of the gold nanoparticles and as a result, ZnO QDs become attached on the gold nanoparticles surface more tightly in the ZnO–Au nanocomposite formation. Therefore, band gap in the ZnO–Au composites decreases with decreasing the size of the gold nanoparticles and in consequence, catalytic activity increases. A lexicon of the apparent association constants, Stern-Volmer quenching constants, band gap and catalytic rate constants for five different sizes of gold nanoparticles in the ZnO–Au nanohybrids are enunciated in Table 6.2. A profile showing the correlation between the values of K_{app}, K_{sv} and K_{cat} with the band gap as a function of particle diameter of gold in ZnO-Au nanohybrids is depicted in Figure 6.10. It is seen that the band gap increases exponentially while the apparent association constants, Stern-Volmer quenching constants and catalytic rate constants decreases exponentially with increase in diameter of the gold particles in ZnO–Au NCs. It is to be noted that apparent

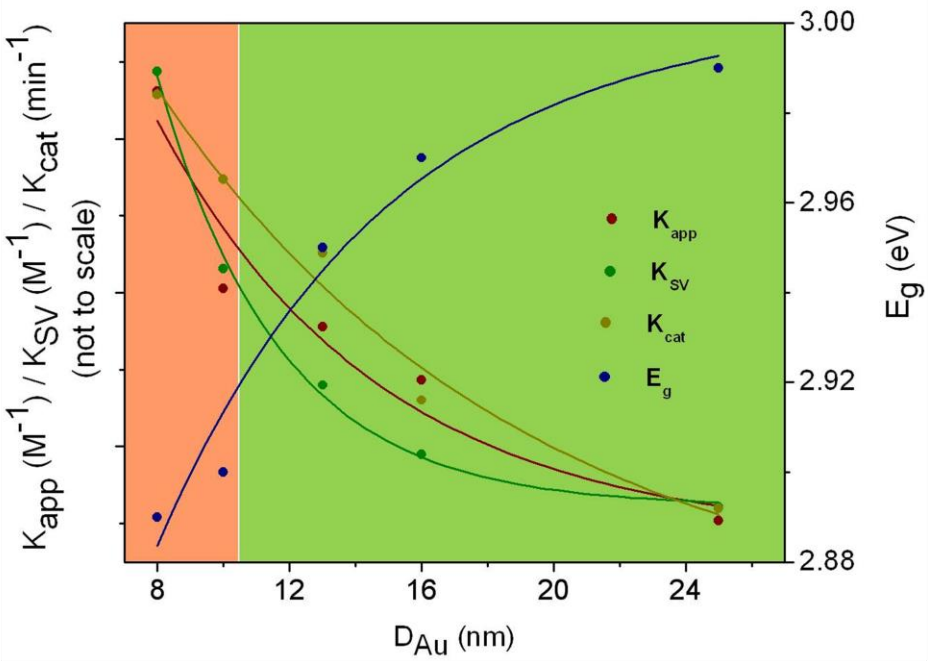

Figure 6.10. Profile showing the correlation between the apparent association constants, Stern-Volmer quenching constants and catalytic rate constants with the band gap as a function of particle diameter of gold in ZnO-Au nanohybrids.

association constants, and Stern-Volmer quenching constants measure the binding affinity of the individual components in maneuvering the hybrid assemblies while the decrease in band gap or catalytic rate constants are the manifestations of the electron transfer at the semiconductor-metal interface. It is evident that there is a significant changes in all the physical properties with the gold particle diameter of *ca.* 10 nm; therefore, Au NPs of diameter less than 10 nm is recommended for engineering the band gap of the ZnO–Au nanohybrids. Moreover, highly reproducible changes in the band gap, apparent association constants, Stern-Volmer quenching constants and catalytic rate constants in similar fashion indicate the specificity of interaction of the metallic and semiconductor components at the nanoscale. It is, therefore, anticipated that smaller gold nanoparticles (≤ 10 nm) prepared by other synthetic methodologies could impart a marked reduction in the band gap of ZnO QDs provided that the metallic particles should possess the chemical binding affinity with the ulrasmall semiconductor particles

6.1.4. Conclusion

In conclusion, the binding of ZnO QDs on the surface of size-specific gold nanoparticles has been investigated in detail that has resolved that the interfacial charge transfer process alters the physicochemical properties of the nanocomposites. The present article demonstrates that the chemical synthesis of water-soluble ZnO-Au nanohybrids that are soluble in aqueous media by simple deposition of ZnO QDs on the surface of gold nanoparticles paves an effective and alternative strategy in comparison with the *in-situ* formation of functional semiconductor-metal hybrid assemblies. Although, pure ZnO QDs exhibit photocatalytic activity towards the degradation of Evans blue but the major disadvantages are the pure ZnO nanostructures could not absorb indispensable amount of visible light; however, this issue can be alleviated, significantly, by combining a semiconductor photocatalyst with tailored plasmonic nanostructures. Moreover, the band gap of the semiconductor-plasmonic metal hybrid assemblies could be miniaturized by changing the size of the gold nanoparticles and the tuneability of the band gap has been probed in the photocatalytic decomposition of Evans' blue under visible light irradiation. Lastly, the simple and facile approach of the present strategy builds a good platform towards fabricating other semiconductor-metal nanohybrids over a wide range of material combinations with morphological anisotropy and functional diversities.

6.2. Tunable Ultraviolet Photoluminescence of Hierarchical ZnO–Ag Assemblies

6.2.1. Introduction

In recent years, with the advent of the art of nanomaterials synthesis, the design of hybrid assemblies by controlled miniaturization of two or more disparate materials represents a potential approach for achieving advanced materials that has become more and more indispensable to fulfill the academic and industrial perspectives.[6,2]Synthetic approaches offering high degree of control over composition and morphology with a wide range of material combinations has become an effective strategy for inducing new physicochemical properties and realizing multifunctionality governed by the synergistic effect among the individual components.[64]The creation of semiconductor–plasmonic metal hybrid assemblies with diverse micro/nanostructures opens opportunities to modulate the optical properties, such as, harvesting, emission or concentration of electromagnetic radiation and produces novel functional materials that will create new avenues, such as, sensing, catalysis, solar energy conversion, optoelectronic devices, fluorescence imaging and diagnosis and therapeutics.[65,4]

Zinc oxide (ZnO) has achieved considerable interest as compound metal oxide semiconductor derived from the group IIb–VI series in the periodic table with the characteristics of wide direct band gap (3.37 eV), large exciton binding energy (60 meV)at room temperature, good thermal and chemical stability, and inexpensive and environmentally friendly due to their biocompatibility.[66]In addition to its numerous inherent physicochemical properties and diverse applications, ZnO displays high optical transparency and luminescent properties in the near UV-vis regions and excellent electrical characteristics, suitable for making sensing devices.[67]Silver particles, in the nanometer size regime, exhibit strong absorption in the visible region; the time-varying electric field of the electromagnetic radiation causes collective oscillation of the conduction electrons in metal nanoparticles with a resonance frequency, often coined as localized surface plasmon resonance (LSPR).[68] Silver nanoparticles have been of interest as the plasma frequency in the visible region overlaps with the emission wavelength of usual energy donors and possess distinctive properties useful for technological

applications in physics, chemistry, biology, and medicine.[68] Therefore, hybrid assemblies comprising of semiconducting ZnO and plasmonic Ag with well-defined architectures have attracted significant interest owing to their potential for providing new opportunities for optimizing, tuning and/or enhancing the optical properties, electronic structure, electrical characteristics, and light-induced charge separation effects.[63,69] The synergistic properties of the ZnO–Ag hybrids have gained considerable attention to study their absorption spectral features,[70] photoluminescence,[41] Raman scattering,[71] second harmonic generation,[72]electrical conductivity,[73]photocatalytic[74] and biological activity.[75]

Numerous innovative approaches have been explored to engender three-dimensional ZnO superstructures, e. g., partial dissociation of water,[76] selective etching,[77]transition metal doping,[78]soft templated synthesis,[79]Kirkendall process,[80] Galvanic-cell-based approach[81] and so on. Herein, we demonstrate a rational approach for the bottom-up assembly into hierarchical ZnO─Ag assemblies possessing intrinsic asymmetry with multiple interesting morphologies. Morphological variation of hierarchical assemblies could be envisaged by tuning the composition of their precursors under alkaline solvolytic condition. The salient feature of materials significance is that a small variation on experimental conditions makes a large difference in the morphology and properties of ZnO–Ag hybrid assemblies. The evolution of the hybrid assemblies has been followed by time-dependent absorption spectroscopy, Fourier transform infrared spectroscopy and X-ray diffraction technique and a plausible mechanism of evolution of the assemblies has been formulated. The optical properties of the as-prepared microstructures reveal the possibility of band gap engineering and tuneability of ultraviolet photoluminescence of the diverse assemblies.

6.2.2. Experimental Section

6.2.2.1. Synthesis of Zinc Oxide-Silver Superstructures using Different Concentrations of Silver Nitrate

The assemblies of zinc oxide have been synthesised using different concentration of silver nitrate in a one pot reaction using a mixture of *o*-xylene and water as the solvent. In a typical synthesis, an amount of 0.055g of $Zn(OOCCH_3)_2.2H_2O$ was dissolved in a mixture of water and *o*-xylene (water: *o*-xylene = 22.5 : 2.5 v/v) in a double necked round bottomed flask by refluxing the mixture in a water bath at 45 °C for 45min. After

dissolving zinc acetate, silver nitrate was added at different concentrations and thus, five different sets of solutions were prepared by varying the concentration (0.4 ─ 1.0 mM) of silver nitrate in the solution. The reaction mixture was, then, refluxed for 15min at 45°C. Subsequently, 13.5 mL methanolic KOH solution (0.1 mM) was added to the reaction mixture and the reaction was kept on refluxing for another 15 min. After that, the temperature was increased to 60 °C and continued for another 1 h. It was seen that, initially, a faint yellow colouration so appeared slowly transformed to curdy white indicating progressive transformation of nuclei into larger particles. The water bath was

Table 6.3. Synthetic Conditions[#] for Different Sets of ZnO–Ag Hybrid Assemblies.

Set	$[Zn(ac)_2.2H_2O]$ (mM)	$[AgNO_3]$ (mM)	$[Zn(ac)_2.2H_2O]$: $[AgNO_3]$	Particle Shape
A	10	1.0	1: 0.010	Cuboidal
B	10	0.4	1: 0.013	Urchin
C	10	0.2	1: 0.020	Multipod
D	10	0.13	1: 0.040	Star
E	10	0.1	1: 0.100	Flower

[#] The binary mixture of water/*o*-xylene was taken in a ratio of 9 : 1 (v/v) and total volume was maintained to 25 mL.

removed and the mixture was stirred for 12h at room temperature. Finally, the zinc oxide-silver assemblies so obtained were retrieved from the solvent by centrifugation at 10,000 rpm for 5minand stored in the dark. A lexicon of the variation of composition of the reactants for the synthesis of zinc oxide–silver particles is summarized in Table 6.3.

6.2.3. Results and Discussion

The manipulation of the concentration of the silver precursor has been found to pave an effective strategy of tailoring the morphology of the hybrid semiconductor-plasmonic metal assemblies. The resultant assemblies so obtained have been characterized by diffuse reflectance spectroscopy (DRS), Fourier transform infrared (FTIR) spectroscopy

cyclic voltammetry (CV), Raman spectroscopy, selected area electron diffraction (SAED) pattern, X-ray diffraction (XRD) pattern and energy dispersive X-ray (EDX) analysis, fluorescence microscopy, transmission electron microscopiy (TEM), high resolution transmission electron microscopy (HRTEM), and scanning electron microscopy (SEM).

The morphology, composition and crystallinity of the particles have been characterized by TEM, SEM, fluorescence microscopic image, EDX analysis and SAED pattern. Typical scanning electron microscopic images, fluorescence microscopic image and energy dispersive X-ray pattern of the ZnO-Ag assemblies are shown in Figure 6.11. Panel (a-e) exhibit the low resolution SEM images of the as-prepared assemblies synthesized in the presence of different concentrations of the silver precursor. It can be clearly observed that variation of the silver precursor concentration in the reaction mixture in the presence of water/*o*-xylene immiscible liquid pairs under solvothermal condition emergent to morphological diversity with specific structural features. Insets in panel (a-e) show the high resolution scanning electron micrographs of the respective assemblies. Closer inspection on the morphology of the assemblies shows that the architectures become more and more complex with increase in the silver precursor

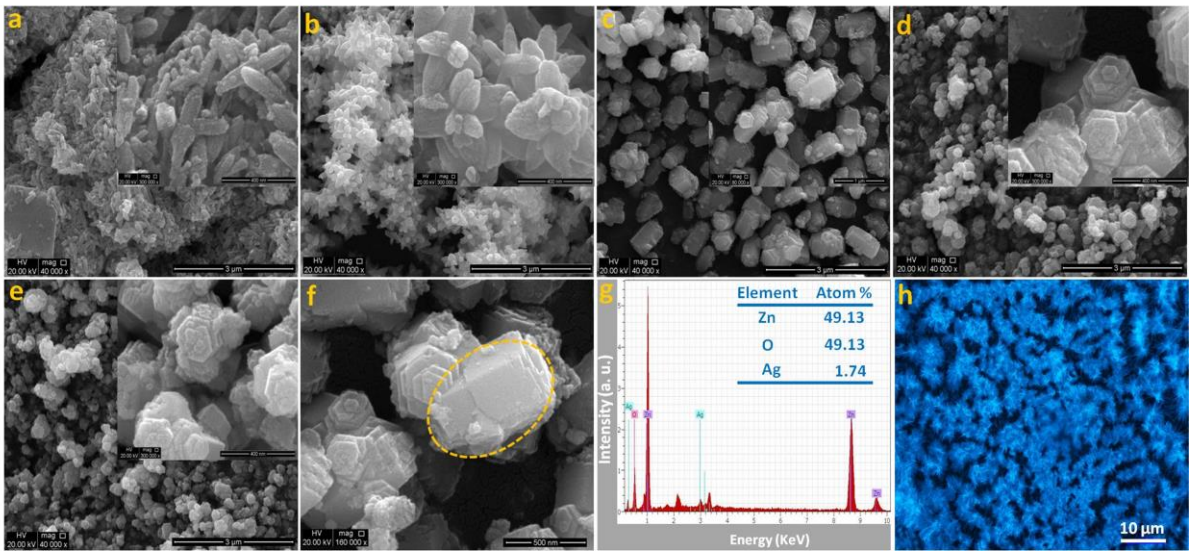

Figure 6.11. (a–e) Scanning electron micrographs of ZnO–Ag assemblies with ZnO: Ag = 1.0 : 0.01, 1.0 : 0.013, 1.0 : 0.02, 1.0 : 0.04 and 1.0 : 0.1, respectively; (f) high resolution SEM image showing the epitaxial growth of sets C, (g) fluorescence microscopic image (set B) and (h) energy dispersive X-ray spectrum (set B).

concentration. More precisely, it is noted that with increase in silver precursor concentration, the variation of the shape of the assemblies from cuboidal-shaped nanorods to urchin-like to multipod-like to star-like to flower-like morphologies becomes apparent. However, it is observed that all these assemblies are well-defined, discrete and nearly uniform throughout their surfaces. From these structural investigations, it is apparent that the concentration of the silver precursor plays a critical role in the evolution of the assemblies through high spatial connectivity.[81]From the representative high magnification SEM image (panel f) of the assemblies (set C), the observation of "broken off" ZnO arms indicates the epitaxial growth of the ultrasmall particles in maneuvering the assemblies.[82] The elemental compositional profile obtained by the representative energy-dispersive X-ray spectrum (panel g) shows the assemblies (set C) are composed of Zn, O and Ag with the atomic ratio of 1 : 1 : 0.035 which confirms the deposition of silver species and absence of other impurities in the as-prepared assemblies.[81] The representative fluorescence microscopic image (in the bright field) of the resultant assemblies (set B) is shown in panel h; the assemblies so formed were collected by micropipette and suspended into water in the cavity of a glass slide. The observation of structurally intact assemblies exhibits the crystallisation of fluorescent ZnO particles into superstructures.[83]

The structural morphology of the as-synthesized assemblies has been, further, confirmed by TEM, HRTEM and selected area electron diffraction pattern as shown in Figure 6.12. Panel a and b show the low-magnification TEM images taken from the edge of the as-prepared ZnO–Ag assemblies of sets A and E, respectively which reveals that the structures are comprised of three-dimensionally spatially connected individual nanocrystals and are smooth and uniform throughout their surface. The substantially higher mass contrast sensitivity in the image causes the silver nanoparticles to appear much brighter than the surrounding ZnO. Panel c shows the HRTEM image of the

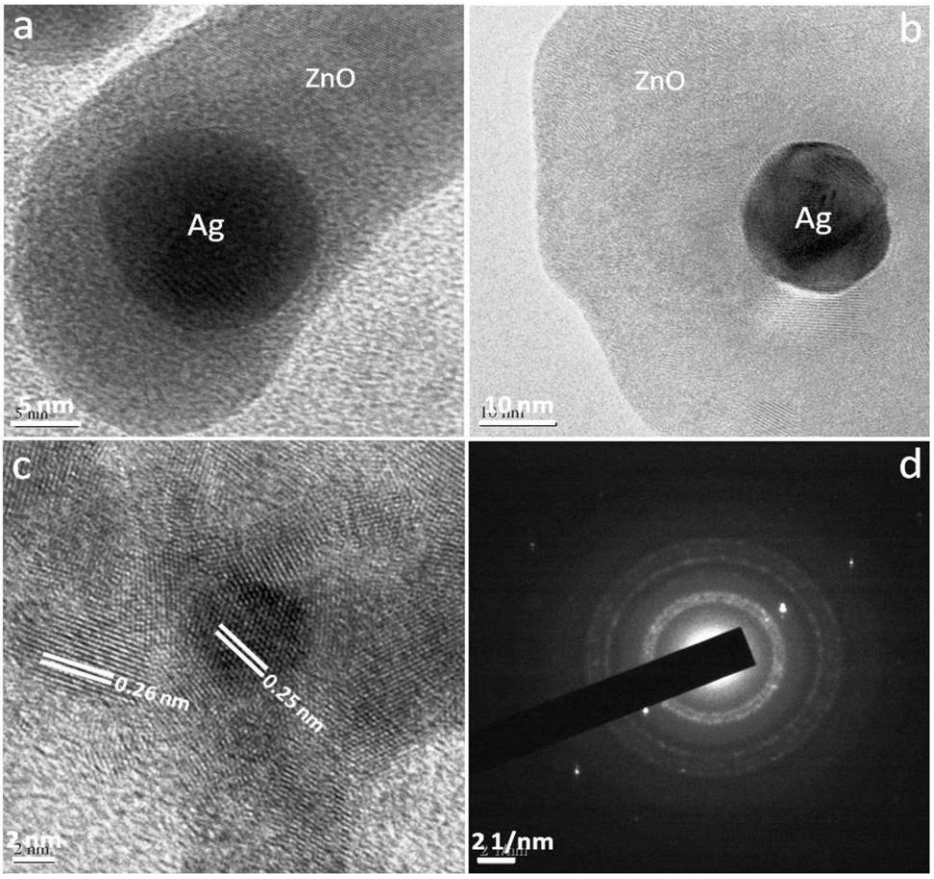

Figure 6.12. (a, b) Transmission electron micrographs of sets A and E, respectively, (c) high resolution transmission electron micrograph of set E and (d) selected area electron diffraction pattern of set E, respectively corresponding to ZnO–Ag assemblies.

ZnO–Ag assemblies (set E) that exhibits the lattice fringes as 0.25 nm belonging to the (111) plane of fcc Ag and 0.26 nm of (002) plane of wurtzite-type hexagonal ZnO at the edge portion, confirming crystalline nature of Ag and ZnO components[84].The corresponding SAED pattern (panel d) of ZnO–Ag assemblies (set E) exhibits the appearance of polycrystalline-like diffraction which are consistent with reflections (100), (002), (101), (102), (110) corresponding to the hexagonal wurtzite phase of ZnO particles along with (111), (200) and (220) diffraction lines of Ag which reveals the crystallographic orientations for both ZnO and Ag in the assemblies.[84]

Since microscopic analysis shows that the as-prepared assemblies are not smooth, the optical absorption of the samples has been measured by diffuse reflectance rather than by normal reflectance. Figure 6.13 shows the diffuse reflectance spectra of the five different

sets of ZnO–Ag assemblies in the solid state. The strong opalescence of the assemblies shows two maxima: one is in the range of 300–350 nm, which is characteristic of ZnO direct band gap transition[66] and other is near 400 nm that arises due to the localized surface plasmon absorption band of the silver nanoparticles.[68]Under plasmon resonance conditions, an evanescent electric field is created at the surface of the nanoparticles that penetrates into the surrounding ZnO and augments the electric field of the illuminating laser.[69]It is seen that although the position of the maximum of ZnO direct band gap transition is different in different sets, the maximum of the silver surface plasmon band is not shifted, significantly, suggesting that the size of the silver domain does not, considerably, with the increase in silver nitrate concentration. However, a regular change in the reflectance spectra was not seen with increase in silver nitrate concentration. The efficiency of concentration of the electromagnetic radiation, critically, depends on the integration of plasmonic and semiconductor units within the composites;[61] therefore, the irregular change in the reflectance spectra can be ascribed to the interplay of different positional and orientational factors of the individual components within the ZnO─Ag assemblies.

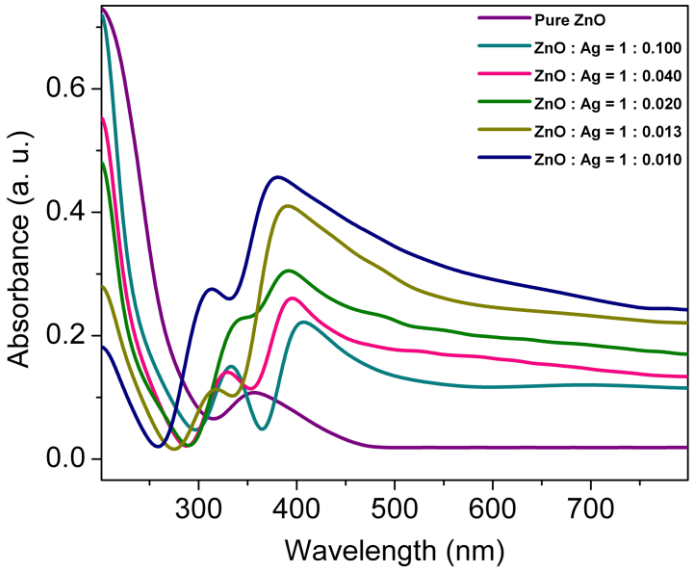

Figure 6.13. Diffuse reflectance spectra of pure ZnO and different sets of ZnO–Ag assemblies.

The engineering of band gap is a common practice for exploiting semiconductors for desired physical properties.[15]The electronic structure of semiconductors, such as, ZnO is characterised by a valence band, which is filled with electrons, and an empty conduction band. In semiconductor–metal composites, the photoinduced charge carriers are trapped by the noble metal particles and become able to promote the interfacial charge–transfer processes.[56]For the purpose of comparison, the spectrum is also included for ZnO particles that were synthesized using the same synthetic methodology except that no

silver precursor was added in the reaction mixture. Figure 6.14 shows the plot of $(\alpha h\nu)^2$ as a function of photon energy ($h\nu$) of the as-synthesized pure ZnO and five different sets of ZnO─Ag assemblies. Although, the band gap of ZnO QDs has been calculated to be 3.96eV, the values of band gap are reduced to*ca.*2.48, 2.45, 2.42, 2.29 and 2.19 eV with increase in silver precursor concentration in consistent with earlier observation.[85] It is, therefore, apparent that manipulating and guiding photons at the microscale inside

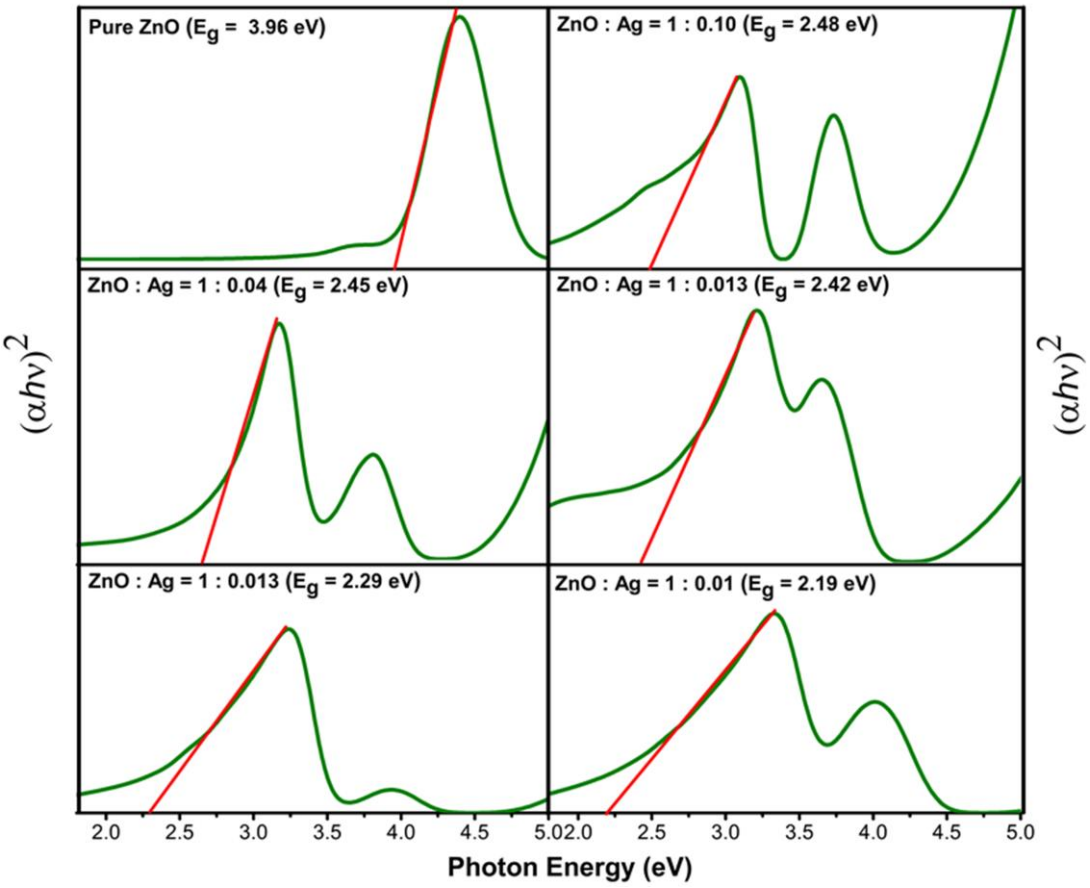

Figure 6.14. Tauc's plot for the estimation of band gap energy of pure ZnO and different sets of ZnO–Ag assemblies.

semiconductor could, sensitively, be managed with the assistance of inter digitated plasmonic metal particles.[33]

Fourier transform infrared spectra of the as-prepared pure ZnO and ZnO–Ag assemblies (set E), recorded in the range 400–4000 cm^{-1}, are shown in Figure 6.15. The FTIR spectrum of pure ZnO(trace a) shows a peak at *ca.* 453 cm^{-1} that can be assigned to stretching vibration of Zn–O bonds; the other absorption band at 1263 cm^{-1} corresponds

to the C–O stretching frequency due to adsorbed acetate counter ions.[86]Upon addition of silver precursor (trace b), FTIR spectrum explicits the appearance of two bands at ~437 and 466 cm^{-1} that can be assigned to the characteristic stretching modes of Ag–O and Zn–O bonds, respectively.[86] Moreover, the presence of extra bands at 1395 and 1663 cm^{-1} could be attributed to the asymmetric and symmetric COO^{-} stretching vibration of acetate chemisorption, respectively, which, probably, accounts for colloid stabilization.[86]The explicit appearance of these bands in the assemblies in comparison with pure ZnO are, possibly, due to large number of ZnO species present in the superstructures. The absorption bands at *ca.* 869 and3165 cm^{-1}arise due to the stretching mode of O–H groups that reveals the existence of a small amount of water chemisorbed and/or physisorbed by the ZnO–Ag assemblies.[86]

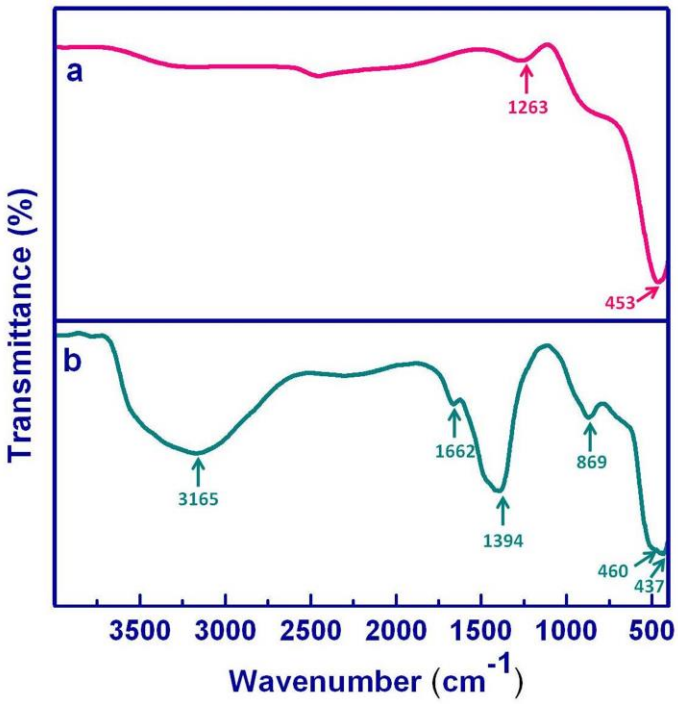

Figure 6.15. Fourier transform infrared spectrum of (a) pure ZnO and (b) ZnO–Ag assemblies (set A).

Cyclic voltammograms of five different sets of ZnO–

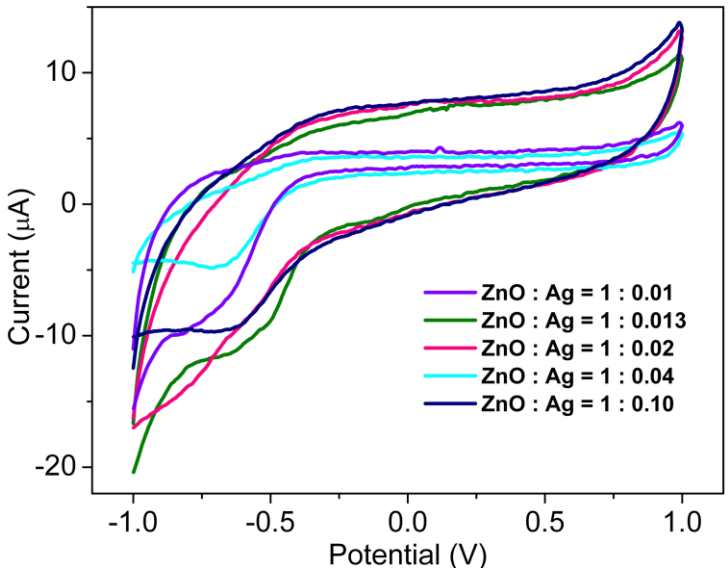

Figure 6.16. Cyclic voltammograms of different sets of ZnO–Ag assemblies (0.01 M).

Ag assemblies (0.01 M) in 0.1 M KCl solution using Ag/AgCl as a reference electrode and Pt electrodes as working and counter electrodes are shown in Figure 6.16. It has been noted that pure ZnO shows the current of 24.99 and 3.67 μA at the potentials of 0.45 and 0.10 V, respectively, whereas, Ag NPs exhibit no peak potentials in the pure state (not shown).From the spectra, is seen that the assemblies do not possess any anodic peak potentials which has been seen for pure ZnO rather a peak at E_{pc} ~ 0.7 V is observed with varying amount of current for different sets of ZnO–Ag assemblies. It is also noted that the amount of current is increasing (4.901, 6.557, 6.584, 8.335 and 10.385 μA for the sets of A–E, respectively) with decreasing the ratio of silver in the assemblies. These results reveal that the electrons become transferred from ZnO to Ag in the heterostructures and as a result, the current is decreasing with increasing the ratio of silver in the hybrid ZnO–Ag assemblies.[86] Moreover, the differences in the flow of current are related to differences in the rate of electron transfer at the interface of the electrodes that reflects the difference in charge densities of different sets of the assemblies.[86]

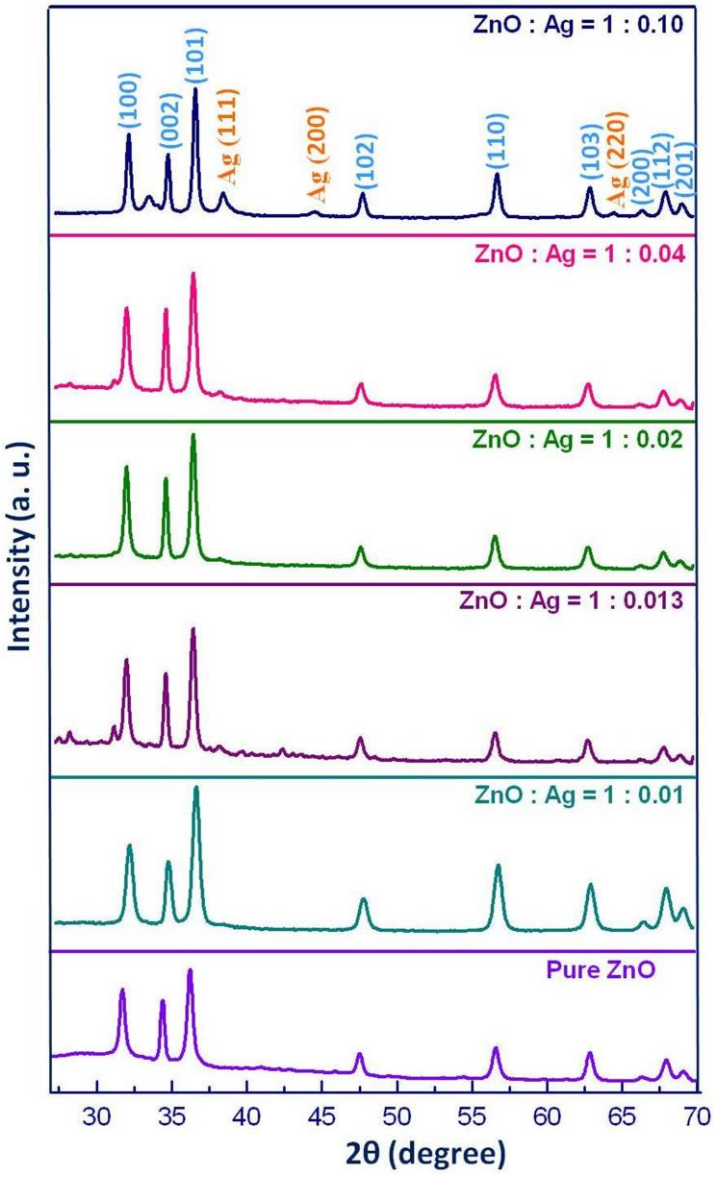

Figure 6.17. X-ray diffraction patterns of pure ZnO and different sets of ZnO–Ag assemblies.

Powder X-ray diffraction patterns of the as-prepared pure ZnO and five different sets of ZnO–Ag assemblies are shown in Figure 6.17. All the diffraction peaks of pure ZnO could be indexed as pure hexagonal phase of Zn with a space group of C_{6v}^{4} and cell constants a = 3.25 Å, and c = 5.21 Å (JCPDS: 76-0704), which suggests that the product comprises ZnO with the wurtzite structure.[87] Upon addition of silver precursor and subsequent hydrolysis in harnessing ZnO–Ag assemblies, in addition to the incipient peaks, additional diffraction peaks at *ca.* 38.1°, 44.3° and 64.47° (JCPDS 87-0597) corresponding to the diffraction lines of (111), (200) and (220), respectively which index as the face-centred cubic of Ag.[87]The appearance of silver peaks becomes prominent with increase in silver precursor concentration; the low intensity of the silver peaks could be attributed to an insufficient concentration of silver in the assemblies.

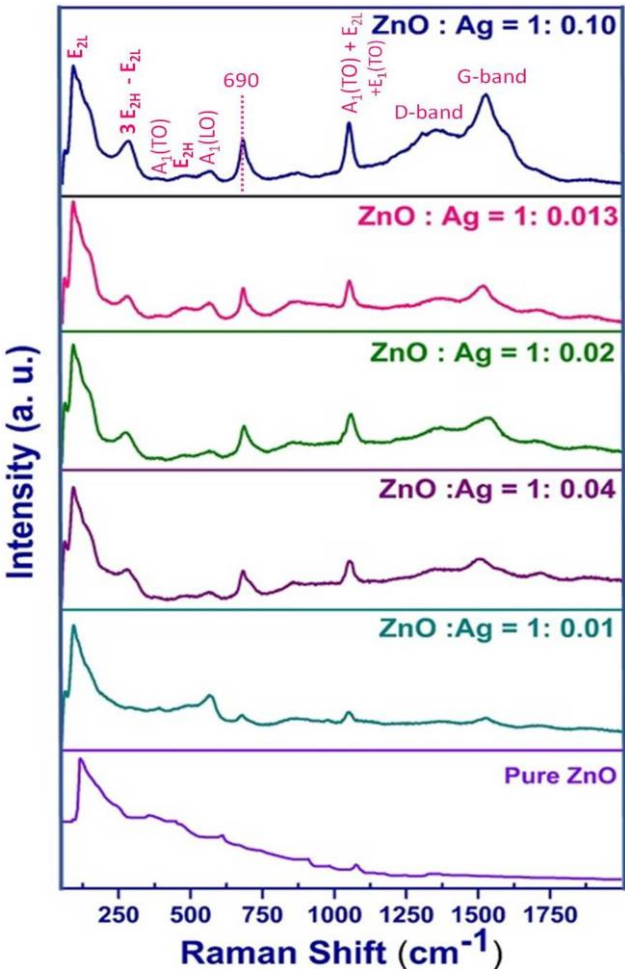

Figure 6.18. Raman spectra of pure ZnO and different sets of ZnO–Ag assemblies.

Raman spectroscopy is the most effective technique to achieve sensitive detection of optical phonon modes and therefore, to characterize related vibrational properties. Figure 6.18 presents the room temperature Raman spectra of pure ZnO and ZnO–Ag assemblies in the 50–2000 cm^{-1}spectralrange; in the present experiment, the samples were excited by the 488 nm line (2.55 eV) of Ar^{+}laser. It is seen that the spectrum of ZnO is very weak; however, the intensity of the peaks increases with increase in silver precursor concentration; surface enhanced Raman scattering is, therefore, observed in the spectrum of ZnO–Ag assemblies. According to group theory,

the structure of ZnO belongs to the C_{6v}^4 symmetry group having two formula units per primitive cell with all the atoms occupying the C_{3v} sites, which predicts eight sets of zone centre optical phonons: two A_1, two E_1, two E_2 and two B_1 modes.

Among these, A_1 and E_1 modes are polar and split into transverse (A_1T and E_1T) and longitudinal (A_1L and E_1L) phonons, all being Raman and infrared active; E_2 modes are non-polar consisting of two modes of low- and high-frequency (E_2L and E_2H) phonons and are only Raman active, and B_1 modes are infrared and Raman inactive (silent modes).[71]The low frequency E_2 mode is observed at 100 cm^{-1}that is associated with the vibration of Zn sub-lattice while the high frequency E_2mode is related to the vibration of only oxygen atoms and is considered as the Raman fingerprint of wurtzite ZnO phase.[71]The A_1(TO) andA_1(LO) polar branches appeared at about 380 and570cm^{-1}, respectively; A_1(LO) phonon mode is commonly assigned to the oxygen vacancies, zinc interstitials, or defect complexes containing oxygen vacancy and zinc interstitial in ZnO.[71]Other two Raman peaks located at about 331 and 1050 cm^{-1} could be assigned to the $3E_{2H}-E_{2L}$ and $A_1(TO)+E_{2L}+E_1(TO)$ multiphonon scattering modes, respectively.[71]TheRaman peak appeared at about 690 cm^{-1} has also been reported for Co-doped ZnO; however, the origin of this peak is, yet, not clear.[88]However, the appearance of two new peaks at 1330 and 1581 cm^{-1}could be attributed to the D-band and G-band of acetate counter ions, respectively, responsible for the stabilization of nanostructures.[89] The appearance of these bands due to acetate counter ions at the higher silver concentration is in conformity with the infrared spectra as discussed earlier.

A reasonable mechanism for the evolution of morphological hierarchy upon increase in the silver precursor concentration as confirmed by multiple control experiments could be enunciated as follows. It has, now, been established that formation of these hierarchical assemblies occurs through the spatial arrangement governed by different intramolecular or intraparticulate interactions, such as, electrostatic interaction, cross-linking agents, hydrogen bonding, charge-transfer interaction, van der Waals forces, dipole-dipole force etc. amongst the individual building blocks.[90] The evolution into hierarchical assemblies was not seen in the absence of silver precursor; therefore, in this synthesis strategy, the *in situ* generated Ag seeds govern the subsequent nucleation of

ZnO, which has a great influence to the final morphologies of ZnO assemblies modulated by silver ion concentration in the reaction mixture. The formation of such ordered assemblies is, also, not observed in the absence of *o*-xylene in the solvent medium; thus, it is apparent that the observed assembly is the result of specific interactions governed by the interfacial tension at the water-organic interface that enable effective interparticle interaction in harnessing the assemblies.[91] Therefore, it could be conceived that the nanocrystals in solution with the well matched crystal lattice and active surface are prone to integrate together through the oriented attachment, driven by the increase of free energy and lattice-free energy.[90] The specific building mechanism of individual components into the assemblies has been investigated in detail by several spatiotemporal experiments, such as, absorption spectroscopy, Fourier transform infrared spectroscopy and X-ray diffraction techniques at different time intervals during the formation of the assemblies as has been presented in Figure 6.19. Panel A shows the time-dependent absorption spectra during the evolution of ZnO–Ag assemblies (set E) after the addition of silver ions. With increase in evolution time, it can, clearly, be recognized that there is an appearance of typical silver plasmon band with a maximum at around 400 nm and consequent changes in the ZnO absorption is seen which indicates the gradual evolution of silver nanoparticles and morphological changes of ZnO in the heterostructures.[69] From

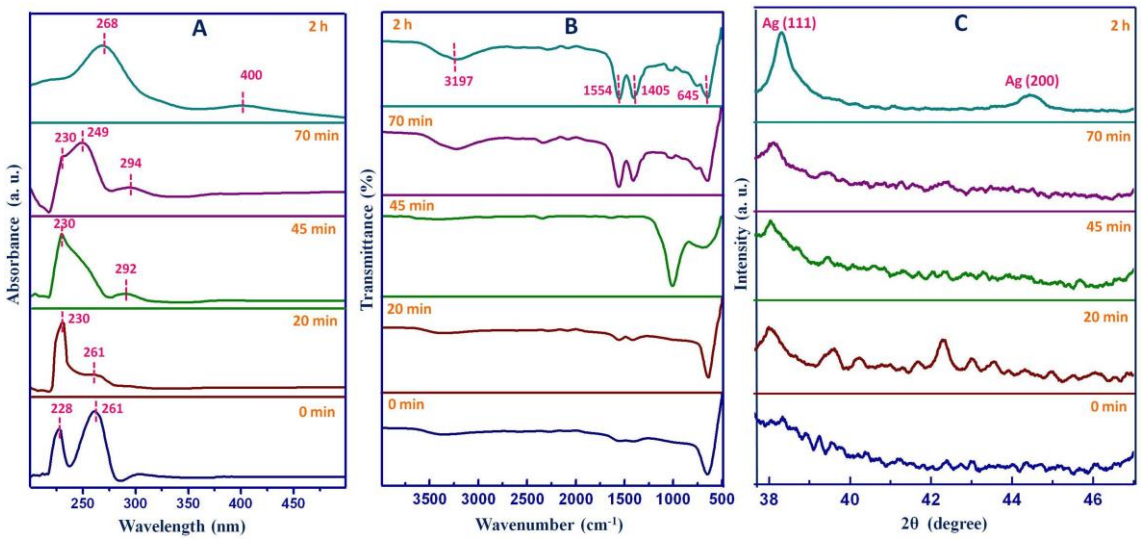

Figure 6.19. Kinetic studies by measuring (A) absorption, (B) Fourier transform infrared and (C) X-ray diffraction pattern showing the evolution of ZnO–Ag assemblies of set E at different time intervals.

the time-dependent FTIR spectra (panel B), the appearance of new bands at ~1405 and 1554 cm^{-1}could be assigned to the asymmetric and symmetric COO^- stretching vibration of acetate chemisorption, respectively.[86]Time evolution of the X-ray diffraction pattern (panel C) show the evolution of two intense peaks corresponding to Ag(111) and Ag(200) and ZnO crystallography becoming progressively more polycrystalline implying ZnO nucleates on the metal nanoparticles suspended in solution and grows thicker as the time progresses. Based on these experimental results, it could be conceived that assemblies are formed as a result of a consecutive and oriented multistage aggregation process and become progressively hierarchical with increase in silver precursor concentration.[92]Therefore, it is manifested that while the liquid-liquid interface offers a viable platform, silver concentration acts as the main architect in maneuvering the hierarchicy in the assemblies.

Hybrid semiconductor-plasmonic metal assemblies have attracted immense interest due to complementarity in the optical properties of the long-lived excitons in semiconductors and the localized electromagnetic modes in metallic nanoparticles that makes it possible to design specific optical responses as a consequence of exciton–plasmon coupling.[93]Therefore, the investigation of structure-luminescence relationship is quite fascinating in shape-selective semiconductor-metal assemblies as has been presented in Figure 6.20. Panel A displays the normalized photoluminescence spectra of pure ZnO and hybrid ZnO–Ag assemblies (λ_{ex} ~ 325 nm) in the solid state. It is seen that all the photoluminescence spectra, mainly, consist of two types of bands: the origin of UV luminescence can be attributed to the photo-stimulated creation of excitons having energies just below the ZnO band edge and their subsequent recombination and the other peak in the visible region may arise from the recombination of photo-generated holes with the electrons in singly occupied oxygen vacancies.[2] It is seen that pure ZnO and ZnO–Ag assemblies exhibit distinctly different emission profile; specifically, the concentration of the silver precursor could tune the photoluminescence properties of the assemblies. Moreover, it is seen that near-band-edge UV luminescence is, progressively, shifted to the red and appearance of new bands in the visible region with increase in silver precursor concentration. The change in the photoluminescence properties of ZnO as a result of the assemblage implicits the strong interaction between the semiconductor

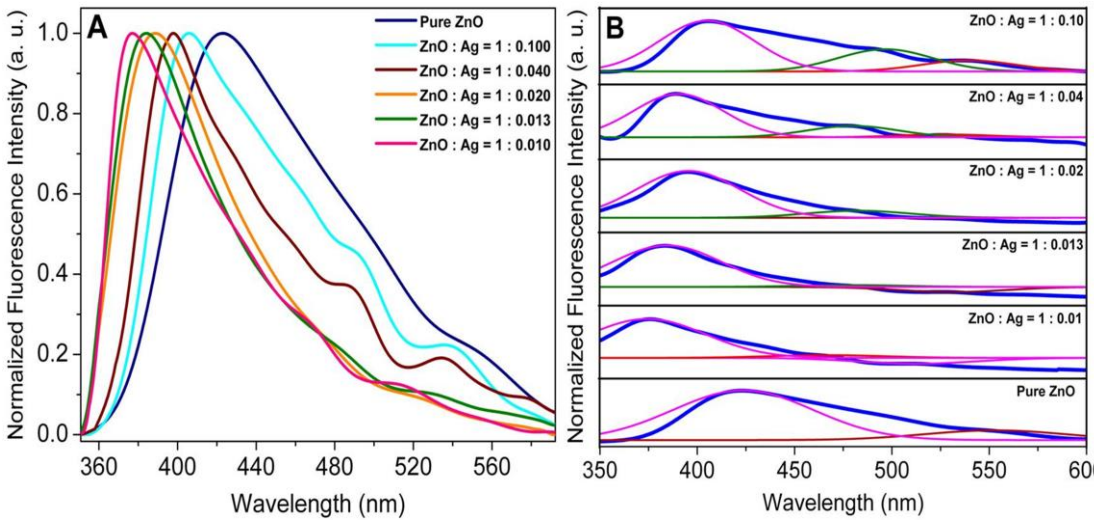

Figure 6.20. (A) Photoluminescence spectra (in the solid state) and (B) deconvolution of the spectra of pure ZnO and different sets of ZnO–Ag assemblies.

and the metallic particles and points to an efficient electron transfer from ZnO to Ag.[87] It has been found that with the increasing Ag doping, the sp-d exchange interaction becomes more dominant due to doping of more d electrons and the difference of Pauling's electronegativity of Ag (1.93) and Zn (1.65). The exchange interactions between electron-electron and electron-impurity give rise to a negative and a positive correction to the energy of conduction and valance bands, respectively, and lead to enhance the band gap of Ag doped ZnO.[94] Gaussian multipeak fitting in panel B explicates the evolution of two visible emission bands in the assemblies, one at 475 nm and another at 525 nm that could be attributed to the presence of oxygen vacancy states on the surface and deep interstitial oxygen states inside the assemblies. This observation implies the involvement of defect-induced energy levels located in the band gap due to the interstitial oxygen ions with increase in silver precursor concentration.[71]

6.2.4. Conclusions

In conclusion, the reported synthetic strategy based on colloidal chemistry provides a facile route to the effective integration of hybrid semiconductor-plasmonic metal assemblies under a unified framework. It has been seen that with increase in silver precursor concentration, the ease and specificity of this dual-solvent thermolytic method provides a rational approach for the bottom-up assembly of complex nanostructures. It has been resolved that the *in situ* nucleation and growth of the Ag domains followed by heterogeneous nucleation and growth of the ZnO component controls their spatial arrangement to induce unique morphology in the assemblies. Such heterogeneous assemblies present not only a natural interface for integrating multiple functions but also exhibit a substantial reduction in the band gap the may lead to the discovery of new properties and functions. The attraction of combining metal and semiconductor nanostructures stems from their complementary optical and electronic properties. Photoluminescence studies elucidates that morphological variation of the ZnO–Ag hybrid assemblies controls both the UV and visible emission that is important to tailor the properties of next-generation bio-nano devices. Findings of this research will help to develop a strategy that is capable of producing micro/nanostructures with desired geometric features and functional properties.

6.3. References

(1) Kadin, A. M.; Burkhardt, R. W.; Chen, J. T.; Keem, J. E.; Ovishnsky, S. R. In *Semiconducting Properties of Amorphous Multilayer Metal-Semiconductor Composites*, Springer-Verlag, USA, 1991, pp. 106–109.

(2) Wang, Y. In *Exciton-Plasmon Interactions in Metal-Semiconductor Nanostructures: Potentials of Controlling Quantum Dot Emissions* Lambert Academic Publishing, Saarbrucken, Germany, 2012.

(3) Mongin, D.; Shaviv,E.;Maioli, P.; Crut, A.; Banin,U.; Fatti, N. D.; Vallée, F. *ACS Nano***2012**, *6*, 7034–7043.

(4) Jiang, R.; Li, B.; Fang, C.; Wang, J. *Adv. Mater.* **2014**, *26*, 5274–5309.

(5) Tran, T. –H.; Nguyen, T. –D. Functional Inorganic Nanohybrids for Biomedical Diagnosis In *Practical Applications in Biomedical Engineering*, Chapter 13, In Tech, Europe, 2012.

(6) Toropov, A. A.; Shubina, T. V. In *Plasmonic Effects in Metal-Semiconductor Nanostructures*, Series on Semiconductor Science and Technology, Oxford University Press, Oxford, UK, 2015.

(7) Wang, Z. L. *Appl. Phys. A: Mater. Sci. Process*. **2007**, *88*, 7–15.

(8) Özgür, Ü.; Alivov, Y. I.; Liu, C.; Teke, A.; Reshchikov, M. A.; Doğan, S.; Avrutin, V.; Cho,S. –J.; Morkoç, H. *J. Appl. Phys.* **2005**, *98*, 041301 1−103.

(9) Eustis, S.; El-Sayed, M. A. *Chem. Soc. Rev.* **2006**, *35*, 209–217.

(10) Daniel, M. C.; Astruc, D. *Chem. Rev.* **2004**, *104*, 293–346.

(11) Dana, J.; Debnath, T.; Maity, P.; Ghosh, H. N. *J. Phys. Chem. C***2015**, *119*, 22181–22189.

(12) Liu, Y.; Zhong, M.; Shan, G.; Li, Y.; Huang, B.; Yang, G. *J. Phys. Chem. B* **2008**, *112*, 6484–6489.

(13) Coppa, B. J.; Fulton, C. C.; Kiesel, S. M.; Davis, R. F.; Pandarinath, C.; Burnette, J. E.; Nemanich, R. J.; Smith, D. J. *J. Appl. Phys.*, **2005**, *97*, 10351 1–13.

(14) Hou, X.; Wang, L.; He, G.; Hao, J. *Cryst Eng Comm*. **2012**, *14*, 5158–5162.

(15) Wu, F.; Tian, L.; Kanjolia, R.; Singamaneni, S.; Banerjee, P. *ACS Appl. Mater. Interfaces***2013**, 5, 7693−7697.

(16) Ong, W. L.; Natarajan, S.; Kloostra, B.; Ho, G. W. *Nanoscale***2013**, *5*, 5568–5575.

(17) Chen, Y.; Zeng, D.; Zhang, K.; Lu, A.; Wang, L.; Peng, D. –L. *Nanoscale***2014**, *6*, 874–881.

(18) Tahir, M. N.; Natalio, F.; Cambaz, M. A.; Panthöfer, M.; Branscheid, R.; Kolb, U.; Tremel, W. *Nanoscale***2013**, *5*, 9944–9949.

(19) Chou, H. –T.; Lin, J. –H.; Hsu, H. –C.; Wu, T. –M.; Liu, C. –W. *Int. J. Electrochem. Sci.* **2015**, *10*, 519–528.

(20) Inakhunbi Chanu, T.; Muthukumar, T.; Manoharan, P. T. *Phys. Chem. Chem. Phys.***2014**, *16*, 23686–23698.

(21) Pacholski, C.; Kornowski, A.; Weller, H. *Angew. Chem. Int. Ed.***2002**, *41*, 1188–1191.

(22) Frens, G. *Nature***1973**, *241*, 20–22.

(23) Kahn, M. L.; Cardinal, T.; Bousquet, B.; Monge, M.; Jubera, V.; Chaudret, B. *Chem. Phys. Chem.***2006**, *7*, 2392–2397.

(24) Ingram, D. B.; Linic, S. *J. Am. Chem. Soc.***2011**, *133*, 5202–5205.

(25) Wang, X.; Kong, X.; Yu, Y.; Zhang, H. *J. Phys. Chem. C* **2007**, *111*, 3836–3841.

(26) Sukharov, M.; Day, P. N.; Pachter, R. *ACS Photonics* **2015**, *2*, 935–941.

(27) Zhang, Y.; Pluchery, O.; Caillard, L.; Lamic-Humblot, A. –F.; Casale, S.; Chabaland, Y. J.; Salmeron, M. *Nano Lett.* **2015**, 15, 51–55.

(28) Aspetti, C. O.; Agarwal, R.; *J. Phys. Chem. Lett.* **2014**, *5*, 3768–3780.

(29) Wood, A.; Giersig, M.; Mulvaney, P. *J. Phys. Chem. B* **2001**, *105*, 8810–8815.

(30) Choi, H.; Chen, W. T.; Kamat, P. V. *ACS Nano* **2012, *6***, 4418–4427.

(31) Shao, R. –W.; Zheng, K.; Wei, B.; Zhang, Y. −F.; Li,Y. –J.; Han, X. D.; Zhang, Z.; Zou, J. *Nanoscale* **2014**, *6*, 4936−4941.

(32) Jakob, M.; Levanon, H.; Kamat, P. V.*Nano Lett.***2003**, *3*, 353–358.

(33) Lu,S.; Qi, J.; Liu, S.; Zhang, Z.; Wang, Z.; Lin, P.; Liao, Q.; Liang, Q.; Zhang, Y. *ACS Appl. Mater. Interfaces* **2014**, *6*, 14116–14122.

(34) Gogurla, N.; Sinha, A. K.; Santra, S.; Manna, S.; Ray, S. K. *Sci. Rep.***2014**, *4*, 6483 1–9.

(35) Bruchez, M.; Moronne, M.; Gin, P.; Weiss, S.; Alivisatos, A. P. *Science* **1998**, *281*, 2013–2016.

(36) Jin, Z.; Gao, L.; Zhou, Q.; Wang, J.; *Sci. Rep.* **2014**, *4*, 4268 1–8.

(37) Aruda, K. O.; Tagliazucchi, M.; Sweeney, C. M.; Hannah, D. C.; Weiss, E. A. *Phys. Chem. Chem. Phys.* **2013,** *15*, 7441–7449.

(38) Otto, S.; Volmer, M. *Phys. Z.* **1919**, *20*, 183–188.

(39) Cheng, C. W.; Sie, E. J.; Liu, B.; Huan, C. H. A.; Sum, T. C.; Sun, H. D.; Fan, H. J. *Appl. Phys. Lett.* **2010**,*96*, 071107 1–3.

(40) Munechika, K.; Chen, Y.; Tillack, A. F.; Kulkarni, A. P.; Plante, I. J. –L.; Munro, A. M.; Ginger, D. S. *Nano Lett.* **2010**, *10*, 2598–2603.

(41) Guidelli, E. J.; Baffa. O.; Clarke, D. R. *Sci. Rep.* **2015**, *5*, 14004 1–11.

(42) Benesi, H.; Hildebrand, J. *J. Am. Chem. Soc.* **1949**, *71*, 2703–2707.

(43) Al-Otaify, A.; Leontiadou, M. A.; dos Reis, F. V. E.; Damato, T. C.; Camargo, P. H. C.; Binks, D. J. *Phys. Chem. Chem. Phys.* **2014**, *16*, 14189–14194.

(44) Förster, T. *Ann. Phys.***1948**, *437*, 55−75.

(45) Hao, E.; Schatz, G. C. *J. Chem. Phys.***2004**, *120*, 357−366.

(46) Lin, T. H.; Chen, T. T.; Cheng, C. L.; Lin, H. Y.; Chen, Y. F. *Opt. Express* **2009**, *17*, 4342–4347.

(47) Noei, H.; Qiu, H.; Wang, Y.; Loffler, E.; Woll, C.; Muhler, M. *Phys. Chem. Chem. Phys.* **2008**, *10*, 7092–7097.

(48) Wang, X.; Andrews, L. *Inorg. Chem.*, **2005**, *44*, 9076–9083.

(49) Sakohara, S.; Ishida, M.; Anderson, M. A. *J. Phys. Chem. B* **1998**, *102*, 10169–10175.

(50) Silva, C. G.; Sampaio, M. J.; Carabineiro, S. A. C.; Oliveira, J. W. L.; Baptista, D. L.; Bacsa, R. ; Machado, B. F.; Serp, P.; Figueiredo, J. L.; Silva, A. M. T.; Faria, J. L. *J. Catal.* **2014**, *316*, 182–190.

(51) Chanaewa, A.; Schmitt, J.; Meyns, M.; Volkmann, M.; Klinke, C.; von Hauff, E. *J. Phys. Chem. C* **2015**, 119, 21704–21710.

(52) Calzolari, A.;Nardelli, M. B. *Sci. Rep.* **2013**, *3*, 2999 1–6.

(53) Sander, T.; Eisermann, S.; Meier, B. K.; Klar, P. J. *Phys. Rev. B* **2012**, *85*, 165208 1–7.

(54) Mao, Z.; Song, W.; Chen, L.; Ji, W.; Xue, X.; Ruan, W.; Li, Z.; Mao, H.; Ma, S.; Lombardi, J. R.; Zhao, B. *J. Phys. Chem. C* **2011**, *115*, 18378–18383.

(55) Zheng, N. F.; Stucky, G. D.*J. Am. Chem. Soc.* **2006**, *128*, 14278–14280.

(56) Dutta, S. K.; Mehetor, S. K.; Pradhan, N. *J. Phys. Chem. Lett.***2015**, *6*, 936−944.

(57) Berezin, M. Y. In *Nanotechnology for Biomedical Imaging and Diagnostics: From Nanoparticle Design to Clinical Applications*, Wiley Interscience, New York, 2014, pp. 312–313.

(58) Antonin, V. S.; Garcia-Segura, S.; Santos,M. C.; Brillas, E. *J. Electroanal. Chem.***2015**, *747*, 1–11.

(59) Patra, B. K.; Guria, A. K.; Dutta, A.; Shit, A.; Pradhan, N. *Chem. Mater.* **2014**, *26*, 7194–7200.

(60) Subramanian, V.; Wolf, E. E.; Kamat, P. V. *J. Phys. Chem. B* **2003**, *107*, 7479−7485.

(61) Achermann, M. *J. Phys. Chem. Lett.* **2010**, 1, 2837–2843.

(62) Ghosh, S. K.; Pal, T. *Chem. Rev.* **2007**, *107*, *4797–4862.*

(63) Khanal, B. P.;Pandey, A.; Li, L.; Lin, Q.; Bae, W. K.; Luo, H.; Klimov, V. I.; Pietryga, J. M. *ACS Nano* **2012**,*6*, 3832–3840.

(64) Korgel, B. A. *Nature Mater.* ***2007***, **6**, 551–552.

(65) Banin, U.; Ben-Shahar, Y.;Vinokurov, K. *Chem. Mater.* ***2014****, 26*, 97–110.

(66) Wang, Z. L. *Mater. Today 2***004***, 7,* 26–33.

(67) Klingshirn, C. *Chem. Phys. Chem.* **2007**, *8*, 782–803.

(68) Liu, X.; Li, D.; Sun, X.; Li, Z.; Song, H.; Jiang, H.; Chen, Y. *Sci. Rep.* **2015**, *5*, 12555 1−7.

(69) Wei, J.; Jiang, N.; Xu, J.; Bai, X.; Liu, J. *Nano Lett.* **2015**, *15*, 5926–5931.

(70) Wang, R.; Yang, W.; Song, Y.; Shen, X.; Wang, J.; Zhong, X.; Li, S.; Song, Y. *Sci. Rep.***2015**,*5*, 91891–14.

(71) Sánchez Zeferino, R.; Barboza Flores, M.; Pal, U.*J. Appl. Phys.* **2011**, *109*, 014308 1–6.

(72) Hyun, J. K.; Kang, T.; Baek, H.; Oh, H.; Kim, D. –S.; Yi, G. –C. *ACS Photonics* **2015**, *2*, 1314–1319.

(73) Kim, A.; Won, Y.; Woo, K.; Kim, C. ─H.; Moon, J.*ACS Nano* **2013**, *7*, 1081–1091.

(74) Liu, H. R.; Shao, G. X.; Zhao, Z. F.; Zhang, Z. X.; Zhang, Y.; Liang, X.; Liu, X. G.;Jia, H. S.;Xu, B. S. *J. Phys. Chem. C* **2012**, *116*, 16182–16190.

(75) Manna, J.; Goswami, S.; Shilpa, N.; Sahu, N.; Rana, R. K. *ACS Appl. Mater. Interfaces* **2015**, *7*, 8076─8082.

(76) Meyer, B.; Marx, D.; Dulub, O.; Diebold, U.; Kunat, M.; Langenberg, D.; Christof, Wll *Angew. Chem. Int. Ed.* **2004**, *43*, 6642–6645.

(77) Zeng, H.; Cai, W.; Liu, P. S.; Kalt, H. *ACS Nano* **2008**, *2*, 1661–1670.

(78) Barick, K. C.; Aslam, M.; Dravid, V. P.; Bahadur, D. *J. Phys. Chem. C* **2008**, *112*, 15163–15170.

(79) Cong, H. ─P.; Yu, S. ─H. *Adv. Funct. Mater.* **2007**, *17*, 1814─1820.

(80) Liu, B.; Zeng, H. C. *J. Am. Chem. Soc.***2004**, *126*, 16744─16746.

(81) Zheng, Z.; Lim, Z. S.; Peng, Y.; You, L.; Chen, L.; Wang, J. *Sci. Rep.* **2013**,*3*, 2434 1─5.

(82) Fan, F. ─R.; Ding, Y.; Liu, D. ─Y.; Tian, Z. ─Q.; Wang, Z. L. *J. Am. Chem. Soc.***2009**, *131*, 12036–12037.

(83) Ali, M.; Pal, S. K.; Rahaman, H.; Ghosh, S. K. ***Soft Matter*** **2014**, ***10***, 2767─2774.

(84) Liu, H. R.; Hu, Y.; Zhang, Z.; Liu, X.; Jia, H.; Xu, B. *Appl. Surf. Sci.* **2015**, *7*, 644−652.

(85) Dong, Y.; Feng, C.; Jiang, P.; Wang, G.; Li, K.; Miao, H.***RSC Adv.*** **2014**, ***4***, 7340–7346.

(86) Huang, J.; Yang, Z.; Feng, Z; Xie, X.; Wen, X. *Sci. Rep.* **2016**, *6*, 24471 1−12.

(87) Aguirre, M. E.; Rodríguez, H. B.; Román, E. S.; Feldhoff, A.; Grela, M. A. *J. Phys. Chem. C* **2011**, *115*, 24967–2497.

(88) Hasuike N.; Deguchi, R.; Katoh H.; Kisoda K.; Nishio K.; Isshiki T.; Harima H.; *J. Phys. Condens. Matter.* **2007**, *19*, 3652231−8.

(89) Valmalette, J. –C.; Tan, Z.; Abe, H.;Ohara, S.*Sci. Rep.***2014**, *4*, 5238 1−8.

(90) Min, Y.; Akbulut, M.; Kristiansen, K.; Golan, Y.; Israelachvili, J. *Nature Mater.* **2008**, ***7***, 527−538.

(91) Grubbs, R. B. *Nature Mater*.**2007**,***6***, 553−555.

(92) Yan, X.; Li, Z.; Zou, C.; Li, S.; Yang, J.; Chen, R.; Han, J.; Gao, W.*J. Phys. Chem. C***2010**,*114*, 1436–1443.

(93) Yin, Y.; Sun, Y.; Yu, M.; Liu, X.; Jiang, T.; Yang, B.; Liu, D.; Liu, S.; Cao, W. *Sci. Rep.* **2015**, *5*, 8152 1−4.

(94) Djurisic, A. B.; Choy, W. C. H.; Roy, V. A. L.; Leung, Y. H.; Kwong, C. Y.; Cheah, K. W.; GunduRao, T. K.; Chan, W. K., Lui, F.; Surya, C. *Adv. Funct. Mater*.**2004**,*14*, 856−864.